

POLITECNICO DI MILANO
Facoltà di Ingegneria dei Processi Industriali
Degree in Materials Engineering and Nanotechnology



ATOMIC LAYER DEPOSITION OF
FERROELECTRIC COMPLEX
OXIDE THIN FILMS

Advisor Dr. Jonathan E. Spanier

Drexel University, Philadelphia, Pennsylvania, United States of America

Co-Advisor Dr. Carlo S. Casari

Politecnico di Milano, Milano, Italia

A THESIS
Submitted to the Faculty in
PARTIAL FULFILLMENT
of the Requirements
for the Degree of
MASTER OF SCIENCE
by:

Brian R. Beatty

Matricola: 780703

Academic Year 2011-2012

© Copyright August 2012
Brian R. Beatty. All Rights Reserved.

For my parents...

Contents

List of Figures	vi
List of Tables	vii
List of Reactions	viii
5 Acknowledgements	xi
Abstract	xiii
Sommario	xv
1 Introduction	1
1.1 Scope of this work	1
10 2 Lead Titanate	3
2.1 Structure	3
2.1.1 Effect of Temperature	3
2.2 Ferroelectricity	4
15 3 Synthesis Methods	7
3.1 Sol-Gel Processing	7
3.2 Metallorganic Chemical Vapor Deposition	7
3.3 Atomic Layer Deposition	7
20 4 Characterization Methods	11
4.1 Compositional Analysis	11
4.1.1 Energy-Dispersive X-Ray Spectroscopy	11
4.1.2 X-Ray Fluorescence Spectroscopy	11
4.2 Thin Film Characterization	12
4.2.1 Variable Angle Spectroscopic Ellipsometry	12
4.3 Phase Identification	15
4.3.1 X-Ray Diffraction	15
4.3.2 Grazing Incidence X-Ray Diffraction	18
4.4 Thermal Analysis	18
4.4.1 Thermogravimetric Analysis	18
4.4.2 Differential Scanning Calorimetry	18

30	5 Sample Fabrication	21
	5.1 Precursor Selection	21
	5.1.1 Titanium Source	21
	5.1.2 Lead Source	21
	5.1.3 Oxidizer	21
35	5.2 Substrate Preparation	22
	5.2.1 Si(100)	22
	5.2.2 Platinized Si(100)	22
	5.2.3 STO(100) and Nb:STO(100)	22
40	5.3 Deposition Parameters	23
	5.3.1 Growth Temperature	23
	5.3.2 Precursor Dosage	24
	5.3.3 Purge Time	25
	5.3.4 Exposure Time	25
45	5.4 Post-Deposition Annealing	25
	5.4.1 Oven Annealing	26
	5.4.2 Rapid Thermal Annealing	26
50	6 Data Collection and Analysis	27
	6.1 Thermal Analysis	27
	6.1.1 Thermogravimetric Analysis	27
	6.1.2 Differential Scanning Calorimetry	27
55	6.2 VASE and Modeling	27
	6.2.1 Data Collection	27
	6.2.2 Model Definition	28
	6.2.3 Analysis Procedure	29
60	6.3 Composition Analysis	32
	6.3.1 Energy-Dispersive X-Ray Spectroscopy	33
	6.3.2 X-Ray Fluorescence Spectroscopy	33
	6.4 X-Ray Diffraction	33
	6.4.1 Grazing Incidence XRD	33
65	7 Results	35
	7.1 Thermal Analysis	35
	7.1.1 Thermogravimetric Analysis	35
	7.1.2 Differential Scanning Calorimetry	36
	7.2 Ellipsometry	36

65	7.3 Composition	36
	7.4 X-Ray Diffraction	36
8	Conclusions	37
	8.1 Future Work	37
	Bibliography	39
70	A Supplemental Information	41
	A.1 List of Chemicals	41
	A.2 List of Samples	42
	A.3 ALD Reactor Diagram	44
	A.4 Recipes for S100 ALD System	45
75	A.5 Thermal Analysis Results	46
	A.5.1 Thermogravimetric Analysis	46
	A.5.2 Differential Scanning Calorimetry	49
	A.6 Composition Results	51
	A.7 Ellipsometry Results	53
80	A.8 XRD Results	58

List of Figures

2.1	Crystal structure of PbTiO ₃	3
2.2	Energy vs. Polarization Plots for FE and PE Materials	4
2.3	Polarization vs. Applied Field Plots for FE and PE Materials	5
85	3.1 Illustration of Example ALD Cycle	8
4.1	Illustration of EDXS principle	12
4.2	Ellipsometric Beam Path and Modeling Parameters	13
4.3	J.A. Woollam M-2000U Ellipsometer	15
4.4	Illustration of Bragg's Law	16
90	(a) Constructive Interference	16
	(b) Destructive Interference	16
4.5	Brüker D8 Discover XRD	17
4.6	Rigaku SmartLab XRD	17
4.7	T.A. Instruments, inc. Instrumentation	19
95	(a) Q50 TGA	19
	(b) Q2000 DSC	19
6.1	Graphical Schematic of VASE Model	29
6.2	Preferred Phase vs. Stoichiometric Ratio	33
100	A.1 Cambridge NanoTech, inc. S100 ALD System	44
	(a) Photograph	44
	(b) Schematic Diagram	44
A.2	TGA Results for Pb(HF ₂ Ac) ₂ Precursor	46
	(a) Mass vs. Temperature	46
	(b) Derivative of Mass vs. Temperature	46
105	A.3 TGA Results for Pb(HF ₂ Ac) ₂ Precursor	47
	(a) Mass vs. Temperature	47
	(b) Derivative of Mass vs. Temperature	47
A.4	Constant Temperature TGA Experiments	48
	(a) Pb(HF ₂ Ac) ₂	48
110	(b) Pb(TMHD) ₂	48
A.5	Results of DSC Experiments	50
	(a) Pb(HF ₂ Ac) ₂	50
	(b) Pb(TMHD) ₂	50

115	A.6 XRF Spectrum of PTO #0	52
	A.7 XRF Spectrum of PTO #20 on Pt-Si	52
	A.8 Results of Ellipsometry on Sample #0	54
	(a) Psi vs. Wavelength	54
	(b) Delta vs. Wavelength	54
	(c) n, k vs. Photon Energy	54
120	A.9 Results of Tauc Analysis on Sample #0	55
	(a) Absorption (α) vs. Photon Energy	55
	(b) Tauc ($\alpha^2 E_{ph}^2$) vs. Photon Energy	55
	A.10 Results of Ellipsometry on Sample #20 on Platinized Silicon	56
	(a) Psi vs. Wavelength	56
125	(b) Delta vs. Wavelength	56
	(c) n, k vs. Photon Energy	56
	A.11 Results of Tauc Analysis on Sample #20 on Platinized Silicon	57
	(a) Absorption (α) vs. Photon Energy	57
	(b) Tauc ($\alpha^2 E_{ph}^2$) vs. Photon Energy	57
130	A.12 Results of XRD Experiments on Sample #20 on Platinized Silicon	58
	(a) Full Range	58
	(b) PTO (100) and PbO ₂	58
	(c) PbO (220) and PTO (200)	58

List of Tables

135	A.1 List of Samples	42
	A.2 XRF Calculated Compositions	51
	A.3 PTO #0 Model Variables	53
	A.4 PTO #20 Model Variables	53

List of reactions

140	Reaction (R 3.1): TMA: Precursor-Surface Site Reaction	7
	Reaction (R 3.2): TMA: Ligand Oxidation & Site Regeneration . . .	7

Acknowledgements

Dr. Jonathan Spanier

Eric Gallo, Dr. Maria Sancho-Torres, Dr. Stephen Nonenmann, Stephanie
145 Johnson, Oren Leaffer, Terrence McGuckin, Guannan Chen, Christopher Hawley

Keith Fahnestock and Professor Caroline Schauer

Rahul Joseph, Dr. Greg Soja

Dr. Amy Peterson and Professor Giuseppe Palmese

150 Other Professors in MATE dept. and Drexel University

Dr. Carlo Casari, as well as Politecnico di Milano

Family and friends.

Abstract

Comments on application of ferroelectric materials.

As devices based on ferroelectric films become more commonplace, a commercially viable process for fabricating the material is needed; low cost and high volume are implied necessities for such a process. This work focuses on the application of atomic layer deposition (ALD) to this task. ALD is a standard fabrication process in the electronics industry, valuable for its high uniformity across large surfaces, capability to control film thickness with very high resolution, and conformality across three dimensional structures. The various tasks in designing and optimizing an ALD process, as well as characterization methods for analysis of the produced films, will be discussed in detail.

Work supported by ARO under Grant #??.

¹⁶⁵ **Sommario**

A detailed summary of the document to be presented solely in Italian.

Chapter 1

Introduction

1.1 Scope of this work

¹⁷⁰ **Chapter 2**

Lead Titanate

2.1 Structure

Lead titanate (PbTiO_3 , PTO) naturally orders into the tetragonal perovskite crystal structure at room temperature (figure 2.1). The structure can
¹⁷⁵ be affected by compositional changes, temperature, or strain (primarily in thin-film systems), allowing a transition to a cubic phase. In the perovskite crystal structure, the central cation (Ti^{4+} in the case of PbTiO_3) is encapsulated in a octahedral cage of anions (O^{2-}), with the remaining cations (Pb^{2+}) situated in the eight corners of the unit cell. If the material was doped (as in a mixed
¹⁸⁰ solid-solution), some of the cations would be replaced with the dopant ions, for example Zr^{4+} would be randomly distributed in Ti^{4+} sites in the $\text{PbTi}_{1-x}\text{Zr}_x\text{O}_3$ (PZT) system.

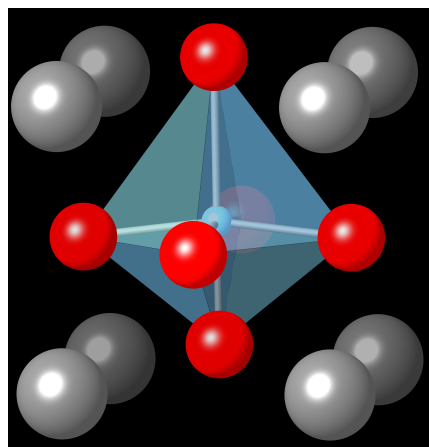


Figure 2.1: Tetragonal perovskite structure of PbTiO_3 .
Grey, red, and blue spheres refer to Pb^{2+} , Ti^{4+} , or O^{2-} , respectively

2.1.1 Effect of Temperature

The transition from tetragonal to cubic perovskite is highly dependent on
¹⁸⁵ temperature. The critical temperature at which this transition occurs is referred to as the Curie temperature (T_C). If the material cools through this

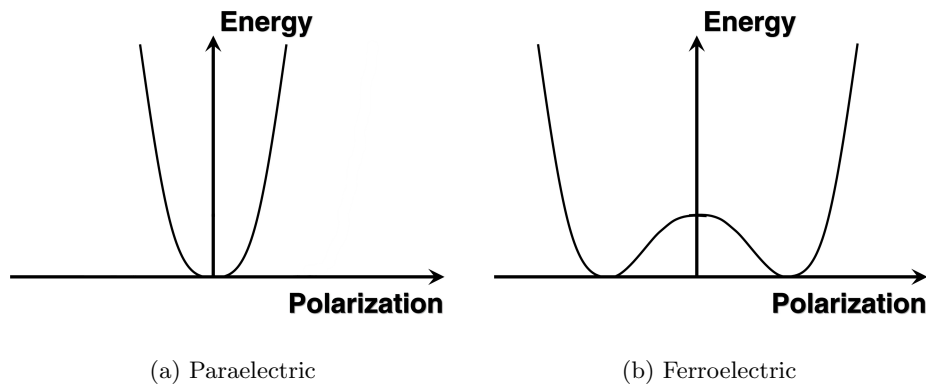


Figure 2.2: Example plots of the energy required to polarize a material. Ferroelectric materials (b) have non-zero polarization at the energy minima. Above T_C all ferroelectric materials transition to a paraelectric phase (a).

temperature, a lengthening of the ‘c’ axis of the unit cell spontaneously occurs. This creates anisotropy in the structure and allows for an anisotropic charge distribution to develop. In lead titanate this is caused by the shifting of the 190 titanium ion, along with a slight shift of some of the oxygen ions as well (visible in figure 2.1 on the previous page). Thus, a permanent dipole is created whose magnitude increases as the system cools further from T_C . This permanent dipole allows the system to exhibit ferroelectricity, implying an ability to semi-permanently switch the orientation of the dipole in the material. This 195 switching can be reversed, but this will not occur spontaneously.

2.2 Ferroelectricity

Ferroelectricity is the capability of a material to exhibit spontaneous electric polarization that requires external influence, such as an applied electric field, to be reversed. This is different from paraelectric (or even dielectric) materials, 200 where there is no polarization without external field being applied. This can be seen in a plot of energy vs. polarization (fig. 2.2) for the two types of materials. In a ferroelectric material, the energy minima are found at non-zero levels of polarization.

One of the most important effects of ferroelectric behavior is the exhibition 205 of hysteresis in the polarization state of the material. **Suboptimal explanations...** Because additional energy is required to make the transition from one

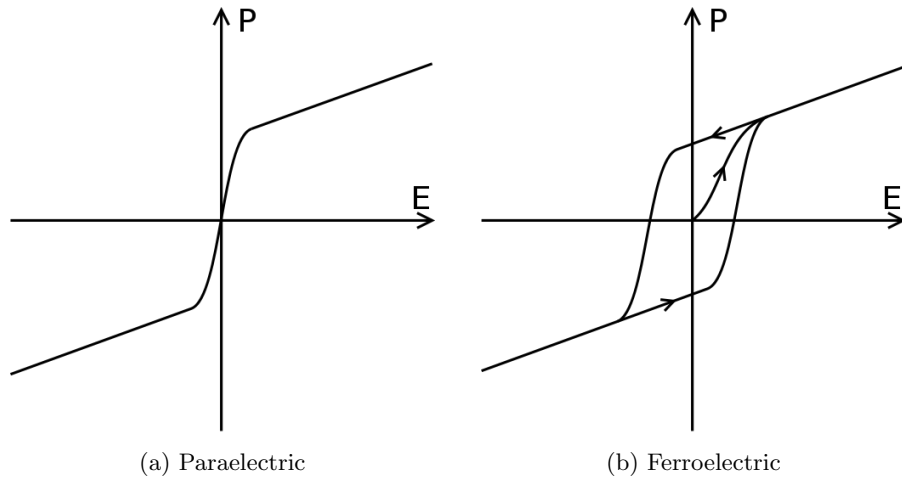


Figure 2.3: Example plots of the energy required to polarize a material. Ferroelectric materials (a) have non-zero polarization at the energy minima. Above T_C all ferroelectric materials transition to a paraelectric phase (b).

state to another, the original state endures for some amount of opposing field (see fig. 2.3b).

Chapter 3

²¹⁰ Synthesis Methods

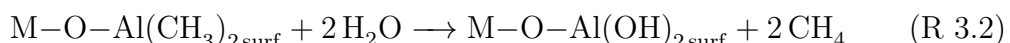
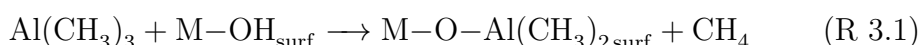
Synthesis of perovskite oxides has been demonstrated using a wide range of techniques. These range from solution-based processing methods (sol-gel approach), to physical vapor methods (molecular beam epitaxy and pulsed laser deposition), and gas phase chemical methods (chemical vapor deposition ²¹⁵ and atomic layer deposition). This review will briefly discuss sol-gel and CVD methodology, but will focus in more depth on films deposited via ALD.

3.1 Sol-Gel Processing

3.2 Metallorganic Chemical Vapor Deposition

3.3 Atomic Layer Deposition

²²⁰ Atomic Layer Deposition (ALD) is a modification on standard CVD processes, with a few major differences. The defining aspect of an ALD process is the separation of the overall reaction into two steps: first the precursor is allowed to react with the substrate surface (see reaction 3.1), excess reactant is purged from the chamber and an oxidizer is introduced to complete the reaction ²²⁵ (see reaction 3.2). These reactions show a very simple ALD reaction between trimethylaluminum (TMA, Al(CH₃)₃) and water.



In this example, it is seen that the first stage allows the TMA to react with the hydrated substrate surface to form part of a layer of alumina (Al₂O₃), liberating a molecule of methane as a byproduct. In the next step, the remaining ²³⁰ ligands are stripped away from the bound TMA molecule and replacing them with hydroxyl groups. This returns the system to the initial state — where the surface is presenting sites available to react with more TMA — and the cycle is completed. A graphical example of this process can be found in figure 3.1.

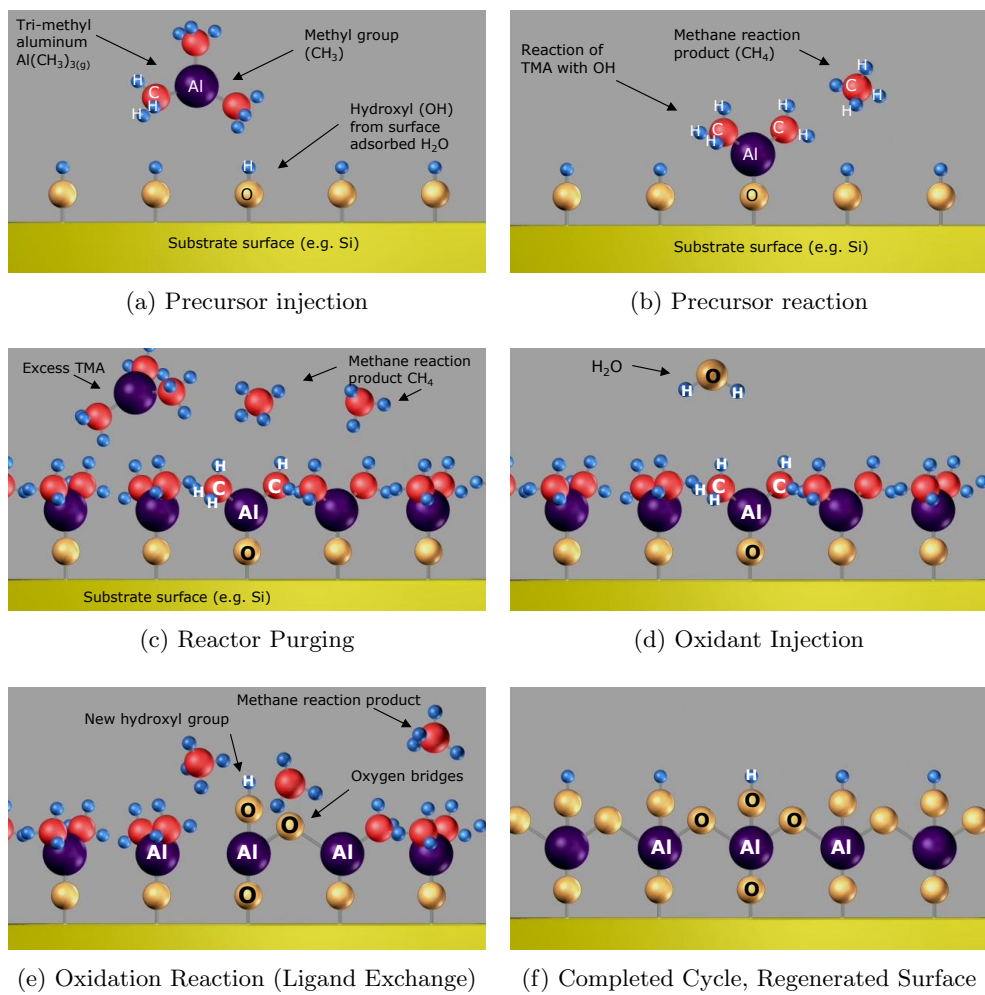


Figure 3.1: Example schematic of the process of an ALD deposition cycle. This example illustrates the reaction of TMA and water to form alumina (Al_2O_3).

Graphic courtesy of Cambridge NanoTech, inc.

Having only surface reactions be permitted, as opposed to CVD where gas-phase interactions dominate, affords ALD a number of unique characteristics.
235 One of these is the concept of the “self-limiting” growth mode. This behavior arises from the limited number of available reaction sites; when all of these have either been reacted with or made unavailable by a blocking mechanism such as stearic hindrance from other local chemisorbed precursor the reaction can
240 no longer proceed. At this point, additional available precursor is not going to be utilized, and instead will be removed and treated as waste material. The system is then evacuated, and a inert purge gas such as dry nitrogen or argon (at UHP grade) is flowed through the reactor. The purge gas serves both to push any remaining gases out of the reactor as well as to help desorb
245 physisorbed species from the surface. If these are allowed to remain adsorbed they would react with the oxidant and negate the surface-limited aspects of ALD. The system would then again be evacuated, and the oxidant introduced and then pumped away to complete the cycle.

In the implementation of most ALD systems, the purge gas is also used as
250 a carrier gas for the precursors. Thus a constant flow of gas is passed through the system, instead of having it occasionally fully evacuated, and the precursor is able to be delivered from its source to the reactor more effectively. For some precursor compounds, in particular those with a low vapor pressure, having carrier-assisted transportation can greatly improve the behavior of the system.

Because of the self-limiting behavior, each deposition cycle is limited to a theoretical maximum of one monolayer of material (in practice a much lower coverage per cycle is attained), which is far less than a unit cell. Generally per cycle growth rates range between 0.03–1.5 Å, with the rate being nearly invariable during most of the deposition. This gives the second defining characteristic of ALD: very high (Å level) thickness resolution. The downside of this aspect is that growths are generally much slower than other types of depositions; ALD is generally slower by an order of magnitude or more than a similar CVD process, as an example. This has proved invaluable in many processes where high precision is critical, such as electronics manufacturing. Intel,
260 for example, uses ALD to deposit extremely thin layers of a high- κ dielectric (such as hafnia, HfO₂) for use as the gate oxide in its transistors, with layer thickness generally less than 2 nm.

This method will produce a layer of a binary oxide material (AO_x), if more complex materials are desired the method must be changed. The basic
270 principles remain the same; one would perform the procedure for depositing a

cycle of a binary oxide and then change the precursor and deposit another cycle of a different oxide material. For example, if one wished to deposit PbTiO_3 , one would begin by depositing a layer of TiO_2 and then depositing a layer of lead oxide (PbO). Repeating this set of cycles — a super-cycle — would
275 eventually form the PbTiO_3 film.

However, deposition of complex oxides is not this simple in practice. In many cases, running each oxide cycle in a 1:1 ratio will deposit a non-stoichiometric material. This makes it necessary to modify the method to deposit more of one type of oxide than the other. For example, if a material is Ti-rich the super-
280 cycle ratio would be modified to increase the number of lead oxide cycles as compared to the titania cycles. Needs more here.

ALD reactions are rather sensitive to a number of factors, such as temperature. The temperature must be high enough that the reactants have sufficient energy to drive the surface reaction but not so high as to allow undesirable
285 reactions to activate (e.g. precursor cracking or surface material desorption). Precursor selection is also very important, for similar reasons. The precursors must also be incapable of reacting with themselves, to allow the self-limiting mechanism to work properly. This section needs more work.

Chapter 4

²⁹⁰ Characterization Methods

4.1 Compositional Analysis

4.1.1 Energy-Dispersive X-Ray Spectroscopy

Energy dispersive X-ray spectroscopy (EDXS) is a commonly used analysis technique for determining the composition of a sample. In this process, a ²⁹⁵ sample is bombarded with high-energy electrons (2–30 keV) which interact with the sample. Some of these electrons will cause a core electron of an atom in the sample to be ejected. This leaves a vacant orbital in the inner shell, which a higher energy electron will fill. In the process of filling the vacancy, the electron will emit an X-ray photon equal to the energy difference ³⁰⁰ between the two states. These energies are referred to using the common X-ray spectroscopy nomenclature (e.g. K_{α} , K_{β} , L_{α}). An illustration of this process can be found in figure 4.1 on the following page.

Since the energies of the emitted photons are very specific to each element, the procedure can be used to identify the presence of the element in the sample. ³⁰⁵ With some calibration, EDXS can also be used to quantify the relative amounts of each element in a sample using the different number of collected photons. However, this can sometimes be difficult due to some elements have overlapping spectrums as the peaks are not sharp and different elements can have similar energies for some transitions.

³¹⁰ One of the downsides of EDXS is that the interaction volume of electrons is much larger deeper into the sample, so the surface sensitivity of the technique is smaller than with some other techniques.

4.1.2 X-Ray Fluorescence Spectroscopy

X-ray fluorescence spectroscopy (XRFS) is a similar technique to EDXS. In ³¹⁵ XRFS the excitation used is X-ray photons (often from a Cu K_{α} source with $\lambda = 1.54 \text{ \AA}$), as opposed to energetic electrons. In other considerations the techniques are equivalent.

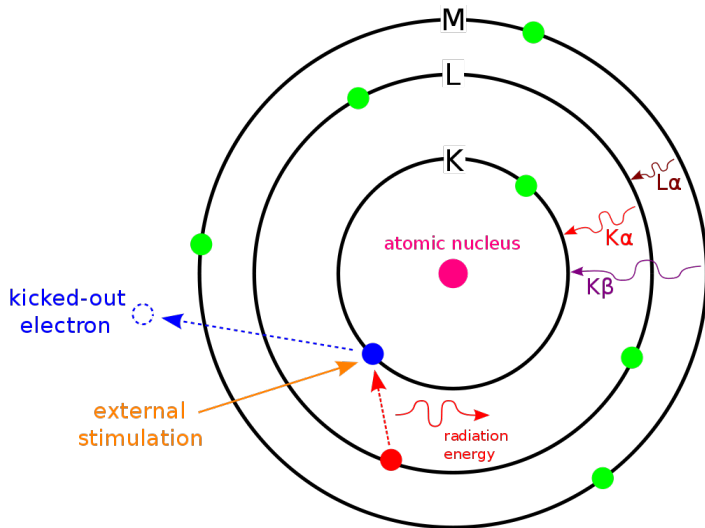


Figure 4.1: Graphic illustrating the basic mechanism for EDXS, along with the commonly used notation for the various energies. The external stimulation would be a high energy electron.

XRFS has a lower noise floor than EDXS, due to the lack of signal from Bremsstrahlung radiation from the deceleration of electrons, allowing smaller signals to be more easily identified (such as in ultra-thin films). It does suffer the same disadvantage of having overlapping peaks. This resolution issue can be alleviated to some degree by using wavelength dispersive XRFS (WD-XRFS), which uses diffraction techniques to analyze the emitted x-ray spectrum.

X-ray fluorescence spectroscopy was performed using a fX-SEM analysis system from iXRF Systems, inc.⁵

4.2 Thin Film Characterization

4.2.1 Variable Angle Spectroscopic Ellipsometry

Ellipsometry is a powerful non-destructive optical technique that allows for the determination of a large number of properties of complex thin film structures. The basic tenet of ellipsometry relies on the analysis of the change in polarization state of a reflected light beam after interaction with the sample. The incident beam is generally linearly polarized, but upon reflection becomes elliptically polarized due to a phase shift in the components of the beam in the s- and p-plane, as well as a change in their relative amplitudes. The phase shift is correlated to the ellipsometric parameter Δ , while the amplitude change is given by $\tan \Psi$ (Ψ is the angle between the s-plane and the major axis of the

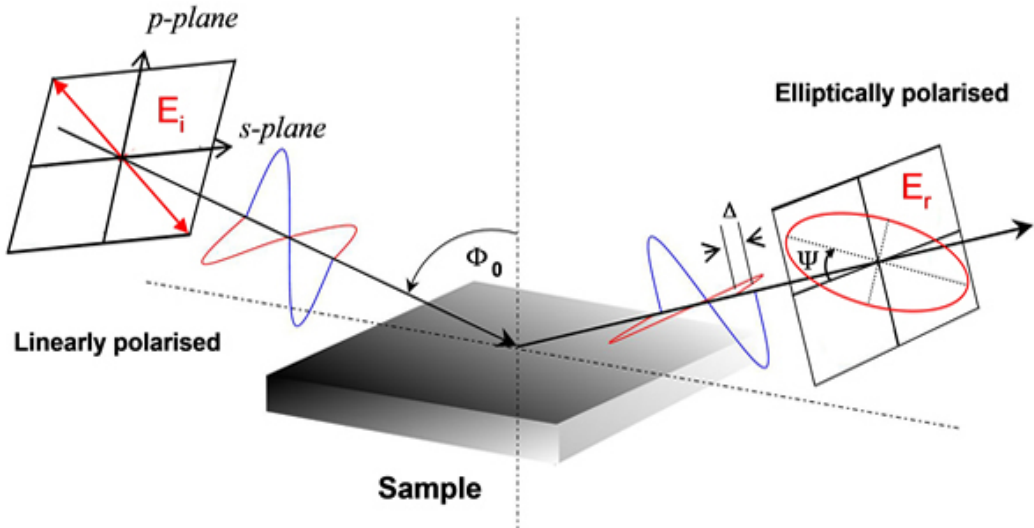


Figure 4.2: Schematic of the beam path during an ellipsometric measurement, critical parameters are indicated

ellipse). The last major parameter is the incident angle, denoted by Φ . A schematic diagram illustrating these parameters can be seen in figure 4.2.

From these parameters, one can directly determine the ratio between the reflectance in the *p*-plane (r_p) and the reflectance in the *s*-plane (r_s) from the fundamental ellipsometric relation (eqn. 4.1). Once this relationship is known, the Fresnel equations (eqn. 4.2) can be used to numerically determine the value of the complex index of refraction at the specific wavelength of the incoming beam. The complex index of refraction (eqn. 4.3 on the following page) describes the nominal index of refraction but additionally includes an imaginary term to describe absorption of light in the material (commonly referred to as the extinction coefficient, κ).

$$\rho = \frac{r_p}{r_s} = \tan(\Psi)e^{i\Delta} \quad (4.1)$$

$$r_p = \frac{\tilde{n}_1 \sqrt{1 - \left(\frac{\tilde{n}_1}{\tilde{n}_2} \sin \Phi\right)} - \tilde{n}_2 \cos \Phi}{\tilde{n}_1 \sqrt{1 - \left(\frac{\tilde{n}_1}{\tilde{n}_2} \sin \Phi\right)} + \tilde{n}_2 \cos \Phi} \quad (4.2a)$$

$$r_s = \frac{\tilde{n}_1 \cos \Phi - \tilde{n}_2 \sqrt{1 - \left(\frac{\tilde{n}_1}{\tilde{n}_2} \sin \Phi\right)}}{\tilde{n}_1 \cos \Phi + \tilde{n}_2 \sqrt{1 - \left(\frac{\tilde{n}_1}{\tilde{n}_2} \sin \Phi\right)}} \quad (4.2b)$$

$$\tilde{n} = n + i\kappa \quad (4.3)$$

This type of analysis is sufficient for thick, isotropic samples without any
 350 surface layers (e.g. surface oxides or adsorbed gases), and can directly provide the value of \tilde{n} . However, once layers are stacked upon one another, the system becomes very difficult to analyze directly due to interference effects between the layers. It becomes necessary to use modeling techniques to determine the correct values of \tilde{n} and thickness (t) for each layer.

The power of ellipsometry as a high-resolution optical analysis technique stems from the use of phase and polarization changes. This allows the analysis to overcome the diffraction limit, and can be accurate down to angstroms. Properly modeling the system is critical for this analysis to be as precise as possible. Thus, there have been refinements of the ellipsometric method to
 360 greatly increase the amount of experimental data points, allowing the overall system to be over-determined and thus letting all of the systems parameters to be calculated.

Variable angle spectroscopic ellipsometry (VASE) is one of these variants. Spectroscopic ellipsometry differs from single-wavelength ellipsometry by utilizing a broad-band light source as opposed to a monochromatic source. By performing ellipsometric analysis at each of the wavelengths, one can determine the wavelength (and thus photon-energy) dependence of n and κ . This not only helps to improve data analysis (as it can generally be safely assumed that the values of n and κ are smooth functions of λ), but allows for the determination of many other properties of the material. Of specific importance is the complex dielectric function ($\tilde{\epsilon}$), which is related to \tilde{n} by the relation shown in equation 4.4 on the next page. Knowing these functions can allow for determination of electronic properties such as the bandgap energy, the absorption coefficient, amongst others. Finally, by obtaining spectra at a number
 370

³⁷⁵ of different incident angles, one directly provides additional data points across the entire wavelength spectrum. Even a small number of additional angles can quickly provide sufficient data points for the system to be over determined.

$$\tilde{\epsilon} = \epsilon_1 + i\epsilon_2 = \tilde{n}^2 \quad (4.4)$$

³⁸⁰ During this project, a VASE M-2000U system (figure 4.3) built by J.A. Woollam, inc. was used to collect all of the ellipsometric data. In addition, data analysis was performed using the WVASE32[©] package also provided by J.A. Woollam, inc. The system utilizes a rotating compensator and a CCD detector to greatly decrease data collection time by collecting data across the entire spectrum simultaneously. More information on this system is available from the J.A. Woollam, inc. webpage.¹

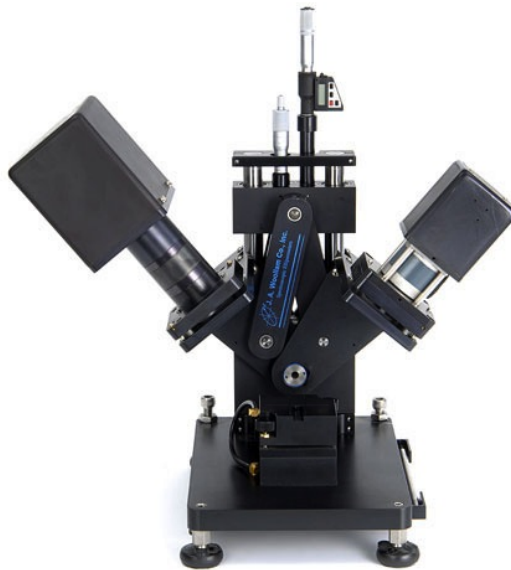


Figure 4.3: Photograph of the J.A. Woollam M-2000U variable angle spectroscopic ellipsometer (VASE)

³⁸⁵ 4.3 Phase Identification

4.3.1 X-Ray Diffraction

Being able to identify the presence of various phases and materials was an important

³⁹⁰ X-ray diffraction (XRD) is a very commonly used technique for performing this identification. Utilizing the concepts of coherent interference, which leads

to Bragg's law of diffraction given in equation 4.5. X-rays are utilized because their wavelengths are similar to the length scales between atomic planes in crystals (1–100Å). As the incident rays pass through the sample and are reflected by atomic planes, they can either constructively or destructively interfere.

$$n\lambda = 2d \sin \theta \quad (4.5)$$

Figure 4.4 gives a graphical illustration of this principle. If the extra distance traversed by photons on the first path is equal to an integer number of wavelengths there will be constructive interference (see fig. 4.4a). However, if the θ angle is slightly changed the interference rapidly obtains destructive character (see fig. 4.4b). In this manner, if the crystal is moved through a range of $\theta - 2\theta$ values, a pattern of angles where constructive interference occurred.

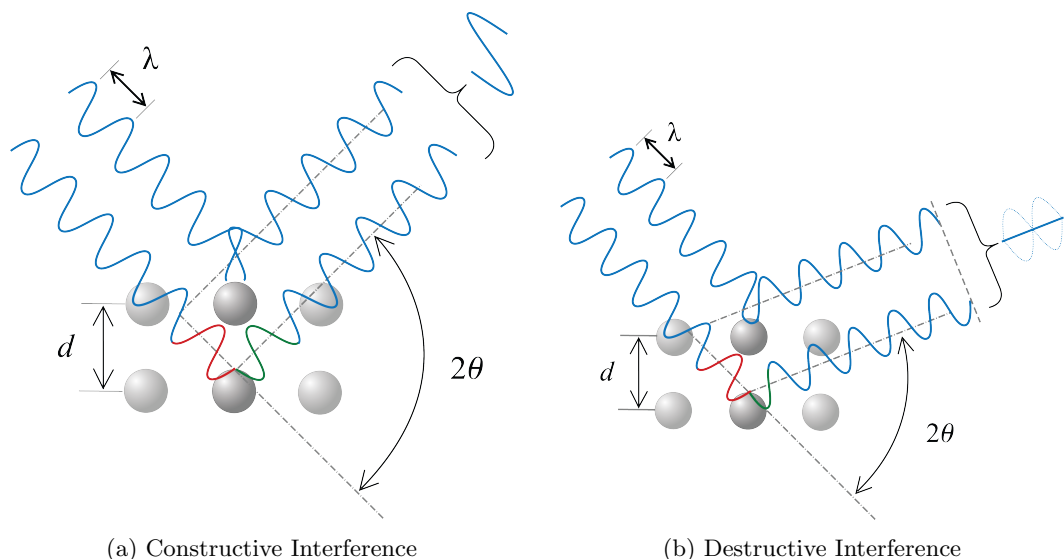


Figure 4.4: These two images illustrate the effect of interference on Bragg diffraction. In (a) the extra path length is exactly correct to allow coherence with the other ray; this causes constructive interference. (b) is the other condition, where the path length causes a phase shift of 90° and thus the rays interfere destructively.

The diffraction pattern can be used to determine a list of the interplane spacings (d-spacings) present in the sample. The values of peaks at various 2θ can be converted to d-spacings via the relation $d = \frac{\lambda}{2 \sin \theta}$. Individual materials will have a specific pattern of reflections that allow them to be identified in the sample.

This project used two XRD instruments, a Brüker D8 Discover XRD and a Rigaku SmartLab XRD (see figures 4.5 and 4.6 on the next page). Both sources utilized a Cu-K α X-ray source ($\lambda = 1.5418\text{\AA}$).

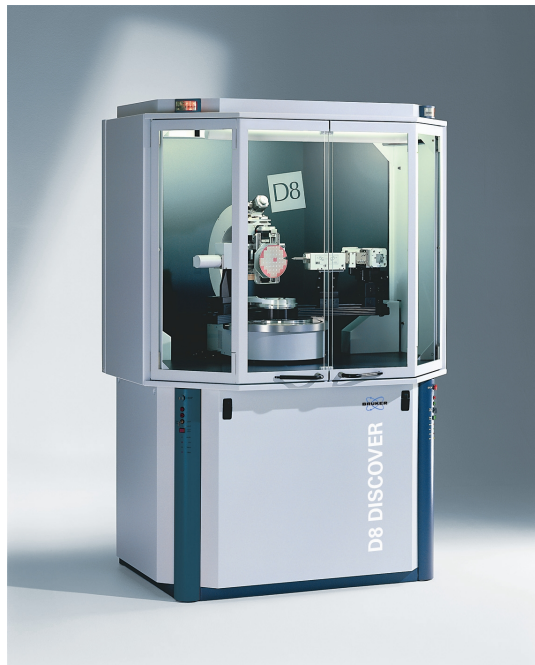


Figure 4.5: Photograph of the Brüker D8 Discover X-ray diffractometer

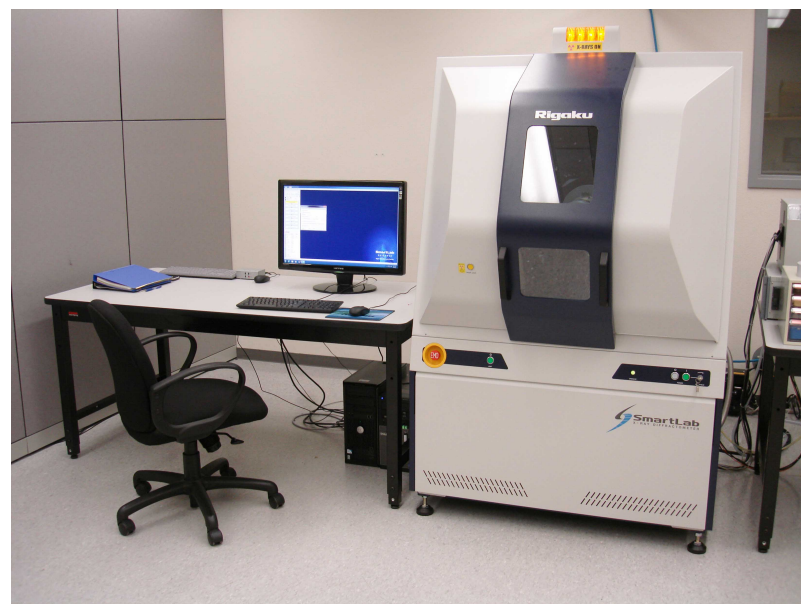


Figure 4.6: Photograph of the Rigaku SmartLab X-ray diffractometer

4.3.2 Grazing Incidence X-Ray Diffraction

410 Both instruments are capable of collected data in GIXRD mode (fixed ω – 2θ).

4.4 Thermal Analysis

4.4.1 Thermogravimetric Analysis

415 Thermogravimetric analysis (TGA) is a very useful tool when attempting to determine the viability of a precursor in an ALD process. It allows for estimation of vaporization rate at various temperature rates as well as indications of chemical breakdown (i.e. thermalization) which would hinder the precursor's usefulness.

420 At its core, TGA is a measurement of mass loss as a function of temperature or time. A small sample (1–10 mg) of material is placed in a microgram balance pan and suspended inside a furnace. The furnace is then heated at a specified rate while the sample mass is carefully monitored. For the experiments used in this study (evaluation of thermal vaporization and thermal degradation) it is important to ensure that the testing environment is inert. This is accomplished 425 by using a platinum pan in the microgram balance and constantly purging the furnace with a small flow of dry nitrogen gas. The heating rate can be varied according to a pre-determined program to provide more information at various individual temperatures.

430 This technique was used to evaluate various precursor candidates for the lead oxide half of the PbTiO₃ deposition procedure. The instrument used was a Q50 TGA device (fig. 4.7a on the facing page). A detailed discussion of TGA procedures and the investigated chemicals can be found in subsequent chapters (see 7.1 on page 35).

4.4.2 Differential Scanning Calorimetry

435 Differential scanning calorimetry (DSC) is a technique that allows for the determination of various critical temperatures for a material, and also can highlight changes in chemical structure due to degradation or other thermal processes.

440 DSC is the analysis of energy absorption as a function of temperature, which is the essence of calorimetry. DSC uses a sample and reference system to isolate the energy absorbed by the sample from that of the holder pan.

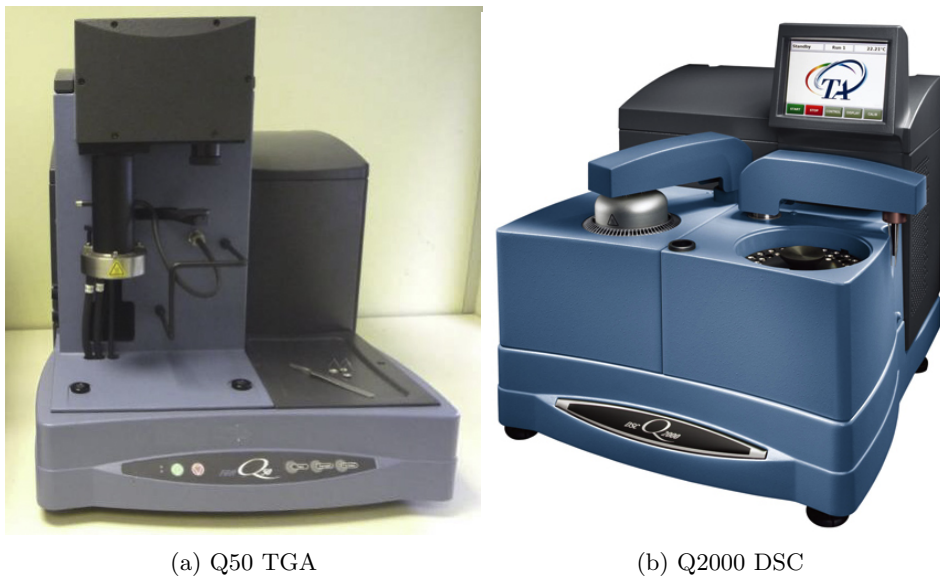


Figure 4.7: Photograph of the thermal analysis instrumentation used during this study, made by T.A. Instruments, inc.

Sample sizes usually range from 0.1–2 mg of material; as the samples used in this study are volatile the sample pans are hermetically sealed to prevent mass loss. The sample and reference pans are then placed inside a thermally insulated chamber. The temperature of each is carefully monitored, and differing amounts of heat are applied to negate the temperature difference between the sample and reference. The difference in absorbed heat as a function of temperature is then given as the result. In general, experiments include both heating and cooling curves to gain a complete understanding of the different energies.

DSC was used to analyze the behavior of precursor chemicals around their evaporation and reaction temperatures. The main goal was to determine if the material underwent any thermally-activated degradation processes at either of these two temperature ranges. At the evaporation temperature, the sample was generally cycled multiple times to simulate actual use in the ALD. These measurements were taken using a Q2000 DSC system (fig. 4.7b) made by T.A. Instruments, inc.

Chapter 5

Sample Fabrication

⁴⁶⁰ 5.1 Precursor Selection

5.1.1 Titanium Source

The source of titanium that was used was titanium(IV) isopropoxide ($\text{Ti}-i\text{-Pr}$, $\text{Ti}(\text{OCH}(\text{CH}_3)_2)_4$). This compound is very commonly used in ALD literature. [Citation needed] It is a liquid precursor with a high vapor pressure ⁴⁶⁵ and reacts easily with most oxidizers; the most commonly used oxidant for this reaction is water vapor, similar to the TMA-H₂O reaction (see section 3.3 on page 7).

5.1.2 Lead Source

Lead sources included bis(2,2,6,6-tetramethyl-3,5-heptanedionato)lead(II) ⁴⁷⁰ (Pb(TMHD)_2) and lead(II) hexafluoroacetylacetone (Pb(HFAC)_2). Both compounds had been referenced in literature [citation needed], were available from multiple chemical suppliers, and were expected to have the highest vapor pressure of the choices available at the time.

Samples of both of these compounds were obtained from Strem Chemical, ⁴⁷⁵ inc. (sp?) Analysis of the precursors included thermal tests (TGA and DSC, see section 7.1 on page 35) as well as test depositions of ALD films.

5.1.3 Oxidizer

Three potential oxidants were considered; these included water, oxygen, and an ozone/oxygen mix. The choice of oxidant depends heavily on the ⁴⁸⁰ reactivity with the potential precursors.

The choice of titanium(IV) isopropoxide as the titanium source allows for any of the three selected oxidizers to be used. A hydrolysis reaction will occur when exposed to water vapor; in the case of oxygen or ozone the ligands will be consumed via a combustion reaction.

⁴⁸⁵ The two lead precursors do not undergo hydrolysis when exposed to water, and as such require the use of the combustion pathway. In addition, it was

found that the reaction proceeded more completely when the O₃/O₂ mixture was used. For simplicity of the process, the O₃/O₂ mix was used for both half-reactions.

⁴⁹⁰ **5.2 Substrate Preparation**

Fabrication and preparation of substrates was an important part of the deposition process. Some substrates were purchased and simply cleaned, others needed to be fabricated or otherwise processed prior to cleaning and use in deposition. Three main types of substrates were used: thermally oxidized ⁴⁹⁵ single-crystalline silicon (100) wafers, silicon wafers that had a thin layer of platinum deposited on the surface, and strontium titanate (100) single crystal substrates.

5.2.1 Si(100)

The silicon substrates were prepared in a simple manner. 4" diameter ⁵⁰⁰ silicon wafers with 200 nm of thermally grown oxide were diced into 1.5 cm x 1.5 cm pieces. When a sample was to be used for deposition, it was cleaned by one minute of sonication in acetone, followed by isopropanol, with a subsequent 5 minutes of sonication in deionized (DI) water. These were then air dried with dry nitrogen. Finally, the substrates were cleaned in a oxygen plasma cleaning system to remove any remaining organic residues present on the surface. ⁵⁰⁵

5.2.2 Platinized Si(100)

Platinized silicon substrates were prepared in a similar manner to the Si(100) samples. For the initial platinization, a large piece of silicon wafer ($5 \times 5 \text{ cm}^2$) was prepared in the manner shown above. Then a 15 nm layer of ⁵¹⁰ platinum was deposited via ALD (deposition recipe can be found in the appendix A.4 on page 45). The substrates were then cleaved into smaller pieces for later use.

If the samples are stored, it is recommended to again clean the samples in the standard procedure prior to use (see [5.2.1](#)).

⁵¹⁵ **5.2.3 STO(100) and Nb:STO(100)**

Oxide crystal substrates were prepared in such a fashion as to promote the formation of atomically flat terraces. This has the advantage of promoting a

uniform surface species across the entire sample — the etchant used in this process leaves the sample titania-terminated.

520 To prepare these samples, the substrates are first pre-cleaned in a three step sonication process. The samples were cleaned for five minutes in each of acetone, methanol, and isopropyl alcohol. Subsequently, the samples were sonicated for fifteen minutes in DI water. Need to find reference and exact timings. Email Eric. The substrates were then dipped into buffered hydrofluoric
525 acid to etch for 35 seconds, then removed and flushed with copious DI water. Once the sample is thoroughly rinsed, the samples are dried using dry nitrogen.

After the etching process, the samples are annealed at 1050°C for two hours. Once the samples are cooled, they are ready for immediate use. AFM can be used to confirm the presence of atomic terraces.

530 If the samples are stored, it is recommended to again clean the samples in the standard procedure (see 5.2.1 on the preceding page).

5.3 Deposition Parameters

535 There are four main parameters that can affect the behavior of an ALD deposition. These are the growth temperature, the dosage of each precursor, the purge time between doses, and any extended precursor-surface exposure time.

5.3.1 Growth Temperature

The temperature of the growth chamber has a strong effect on reaction behavior. ALD reactions are sensitive to temperature, and will only proceed
540 properly within a certain range known as the ‘ALD window.’ Outside of this range, the reaction enters one of a number of different regimes; these are determined by comparing the growth rate of the deposition to that of a reaction in the self-limiting saturated “ALD mode.”

If the growth temperature is less than the lower bound of the ALD window, the two regimes are condensation limited and activation energy limited.
545 Condensation limited growth occurs when the substrate temperature is low enough that precursor condenses onto the surface without reacting with the presented sites. This causes higher than expected growth rates, and a lack of self-limiting behavior. If the reaction instead proceeds into the activation

550 energy limited regime, molecules of precursor lack sufficient energy to react with the surface. This is characterized by lower deposition rates.

Conversely, if the reactor temperature is excessive the reaction again become anomalous. Decomposition limited growth, characterized by excessive deposition, is a result of thermal cracking of the precursor materials. This reaction is not limited to the surface, and accounts for the extra material being deposited. Lower deposition rates indicate that the temperature is sufficient to cause desorption of previously-reacted material from the sample.

For an ALD run to be successful, the acceptable temperature window for all of the reactions should overlap in some temperature range. This can become difficult with reactions requiring multiple metal precursors (e.g. PbTiO_3 , a combination of TiO_2 and PbO), as these can have widely varying ALD windows for their respective reactions.

5.3.2 Precursor Dosage

The dosage of precursor or oxidant to the surface is another parameter of critical importance. An ALD reaction requires a minimal amount of precursor to sufficiently saturate the surface, while it is beneficial to minimize any excess precursor as it will be a wasted byproduct (minimizing costs, environmental impact, etc.).

The vaporization behavior of the precursor can have a dramatic impact on how simple or difficult it is to deliver a saturating dose to the surface. Some materials have readily available precursors with high vapor pressures; titanium isopropoxide and trimethylaluminum (TMA) are both liquids, and tetrakis(dimethylamido)hafnium ($\text{Hf}\{\text{N}(\text{CH}_3)_2\}_4$) is a low-melting temperature solid. These are commonly used precursors for depositing their respective oxides. This vapor pressure becomes an important consideration when choosing a potential compound for use in ALD (as discussed in section ?? on page ??).

Insufficient dosing is apparent in a deposition run by a slower than average growth rate, or also as a non-uniform deposition rate across the sample. However, overdosing is not readily apparent in an ALD-mode deposition. The dose must be lowered to a point where the dose is insufficient, and then increased back to a saturating level.

Controlling the dose is dependent on injection time (which is the time the valve between the process line and the precursor storage vessel is open), precur-

585 sor temperature, and the cycle duration (time between precursor injections). By increasing either the injection time or the precursor's temperature the dose is increased, except in some cases with low vapor pressure materials. In this case, it can sometimes be found that the evaporation kinetics are slow and it takes additional time to build up a sufficient amount of vapor to provide a
590 dose to the reactor.

If necessary, multiple doses of precursor can be delivered to the sample during each cycle to increase the total delivered dose.

5.3.3 Purge Time

Purge time is important as it gives time for the N₂ flow to flush any remaining byproducts and excess reactants from the reactor zone. It also allows time between cycles which allows for low vapor pressure precursors to regenerate evaporated material; if this time is too short to fully regenerate the dose in the cylinder the precursor will eventually appear to be depleted during the course of the deposition.
595

600 5.3.4 Exposure Time

Exposure time denotes the time where the precursor is held in the reaction zone to increase the amount of time during which the surface reaction can occur. This is beneficial for two types of depositions. In the case of low-reactivity precursors, it increases the amount of time that the precursor is available to the surface, greatly increasing the surface coverage per cycle. Exposure mode is also beneficial for depositing upon three dimensional structures, especially those with a high aspect ratio, e.g. nanotube templates. This extra dwell time of the precursor allows for diffusion of reactant into the structure, for a uniform coverage upon the entirety of the surface. Purge time must be increased
605 accordingly to allow for byproducts to diffuse back out of the structure.
610

5.4 Post-Deposition Annealing

Two types of annealing procedures were used in this study. Oven annealing, with the simple use of a furnace in ambient atmosphere; and rapid thermal annealing (RTA), characterized by very high heating and cooling rates and
615 performed in an inert atmosphere (dry N₂).

5.4.1 Oven Annealing

5.4.2 Rapid Thermal Annealing

Chapter 6

Data Collection and Analysis

6.1 Thermal Analysis

6.1.1 Thermogravimetric Analysis

6.1.2 Differential Scanning Calorimetry

6.2 VASE and Modeling

Ellipsometry was used extensively to determine a variety of properties of the material. However, the primary goal of ellipsometric analysis was to determine the film thickness, in order to be able to determine the film growth rate (in terms of Å per deposition cycle) of the process.

6.2.1 Data Collection

In order to collect the experimental data, the following series of steps were followed:

1. Optics alignment
2. Ambient light compensation (DC offset)
3. Data collection at multiple angles

Alignment of the optics of the system is performed in the manner described in the manual for the ellipsometer.² The system can have focusing optics installed which diminish the spot size of the analysis, which is useful if inhomogeneity is expected in the sample as this is a major problem for analysis (two of the main assumptions made by ellipsometric models are that the layers have consistent thicknesses and optical behavior across the analysis area). This is done by manually adjusting the sample stage height and the sample surface plane. The system is designed so that when the incoming signal is maximized the sample is properly aligned with respect to the p- and s-planes defined by the equipment.

Once the system is aligned, the signal that is due to ambient light (not produced by the light source) must be compensated for. The M-2000U defines this as the “DC offset.”² The offset is calibrated automatically by the system by blocking the light source and measuring the signal from the surroundings. As the light present in the room is generally randomly polarized, the signal will be invariant to the polarizer settings. Correctly setting this value greatly decreases the uncertainty during the analysis phase; it mainly affects the degree of light depolarization measured by the system. The ellipsometer includes the depolarization in its calculation of the confidence interval for the final measurement. If the degree of ambient unpolarized light is not determined before the measurement, the depolarization will be nearly completely unrelated to the actual depolarization by the sample. In addition, the depolarization can be used by non-idealized models to determine such parameters as layer thickness variation, or internal interface roughness. This process will not be used for the remainder of this discussion, but more information can be found in the manual for the M-2000U.²

After the calibration steps have been completed, data collection can be performed. Three different incident angles were used for the data collection: 55°, 60°, and 65°. At each angle, the data was averaged over three hundred revolutions of the compensator to minimize noise in the experimental data. The system was set up to collect depolarization data simultaneously with the ellipsometric parameters.²

If the sample is expected to be inhomogeneous, the focusing optics can be used and data collected at several different locations on the sample. This can provide data on how the growth process behaves spatially, such as if there is abnormal growth near the edges of the sample but homogeneous deposition as one moves nearer to the center of the substrate.

6.2.2 Model Definition

The definition of the model is a critical part of the analysis procedure. The model dictates how the software package will perform its various calculations to predict the overall optical behavior, which it iteratively compares to the experimentally determined Ψ and Δ .

Simply put, the model is defined as a bulk (semi-infinite) substrate layer, with a nominal number of nano- to micrometer thick layers stacked upon it. Each layer is modeled with a prediction of optical constants at each test wave-

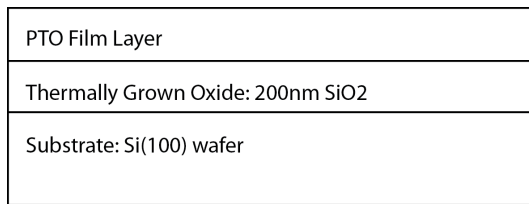


Figure 6.1: A simple graphical example of the model used for analysis of the film stack in the Si(100) samples. The parameters are t and the spectroscopic values of \tilde{n} for the PTO layer.

length. These optical constants can be provided as a table of experimentally
680 determined results, which are available for many commonly used materials such as silicon, silica, titania, amongst others; they can also be predicted using a variety of different models. These can be empirical predictors, such as the Cauchy dispersion, or based upon physical properties of the material, oscillator-based models for example. The model types relevant to this work
685 are discussed in more detail in subsequent sections.

The four different substrates require different material layer stacks to properly represent them, and each poses individual challenges for characterization. The Si(100) substrate that was most commonly used for this work was the simplest to model. It can be represented as a substrate layer of silicon, with
690 a 200 nm layer of silica on top. The deposited film would be layered above the SiO₂ layer (see fig. 6.1 for a schematic representation). A large number of these substrates were analyzed for their oxide layer thickness, where the only parameter to be fit was the layer thickness. It was found that the nominal oxide layer was 200 ± 5 nm thick. This was consistent enough that 200 nm could
695 be used for the initial thickness estimate for all samples using this substrate, and after the ALD layer was analyzed this thickness could also be included in the fit to confirm the true dimensions of the oxide layer. The substrate with thermally-grown oxide was preferred in comparison to silicon with only native
700 oxide layer; this is because the thicker layer of transparent oxide helps to generate large oscillations in Ψ and Δ , which assists in the analysis (particularly the thickness, where the fringes are very closely related to this parameter).

6.2.3 Analysis Procedure

Once the data was collected, a specific series of steps was followed in order to obtain the highest degree of accuracy from the model. All steps were performed
705 on the PTO layer. The procedure went as follows:

1. High- λ Cauchy Model
2. Direct Calculation of n and κ
3. Conversion to Oscillator Model
4. Refinement of Oscillator Layer Parameters

This first step takes advantage of the transparency of the film at high wavelengths (low energies) where the photon energy is below the optical bandgap of the material. In this region, the Cauchy model can be used. The Cauchy model is empirical rather than physically descriptive, and best used for amorphous materials such as polymeric films, however the assumptions required for reasonable accuracy are met when absorption in the film layer is minimized (therefore $\kappa(\lambda) \approx 0$). The equations used in the Cauchy model are shown in equation 6.1. Generally, analysis during this step was performed in the spectral region where $\lambda = 600 - 1000$ nm ($E_{ph} = 2.06 - 1.24$ eV).

$$n(\lambda) = A_n + \frac{B_n}{\lambda^2} + \frac{C_n}{\lambda^4} + \dots \quad (6.1a)$$

$$\kappa(\lambda) = A_\kappa e^{B_\kappa \left(\frac{hc}{\lambda}\right) - C_\kappa} \quad (6.1b)$$

Once reasonable estimates for n , κ , and the film layer thickness are obtained at the higher wavelengths, the second step of the analysis is to generate values of \tilde{n} for the rest of the spectrum. The film thickness parameter is fixed at the value determined from the Cauchy model. The values of n and κ are allowed to be determined freely without the use of a model (i.e. directly determined by use of the Fresnel relations). This type of modeling is not physical, but assists in the generation of the oscillator-based model in the next step. The software package is then instructed to run a point-by-point fit of the data from highest-to lowest- λ , attempting to minimize the change in n or κ between adjacent data points.

This model is then inputted into a oscillator model. For the analysis of these films, a Tauc-Lorentz oscillator model was utilized. The oscillator models used by WVASE32 are expressed in terms of the complex dielectric function $\tilde{\epsilon}$, which relates to \tilde{n} via the relationship in equation 6.2 on the next page. The Tauc-Lorentz model changes the Lorentzian model by allowing for some absorption below the fundamental bandgap energy, which would be due to defect states and other intra-band transition mechanisms. The Tauc-Lorentz

model uses the parameterization shown in equation 6.3.^{2,3} ϵ_1 is provided here in a condensed version (eq. 6.3a); the full expanded version, and its derivation via Kramers-Kronig integration (whose relations are shown in equation 6.4) from ϵ_2 , has been presented by Jellison and Modine.³

$$\tilde{\epsilon} = \epsilon_1 + i\epsilon_2 = \tilde{n}^2 \quad (6.2a)$$

$$\epsilon_1 = n^2 - \kappa^2 \quad (6.2b)$$

$$\epsilon_2 = 2n\kappa \quad (6.2c)$$

$$\epsilon_1 = \frac{2}{\pi} P \int_{E_g}^{\infty} \frac{\xi \epsilon_2(\xi)}{\xi^2 - E^2} d\xi \quad (6.3a)$$

$$\begin{cases} \epsilon_2(E) = \frac{AE_0C(E - E_g)^2}{(E^2 - E_0^2)^2 + C^2E^2} \cdot \frac{1}{E} & E > E_g \\ \epsilon_2(E) = 0 & E \leq E_g \end{cases} \quad (6.3b)$$

$$(6.3c)$$

740

$$\epsilon_1(\omega) - 1 = \frac{2}{\pi} P \int_0^{\infty} \frac{\omega' \epsilon_2(\omega')}{\omega'^2 - \omega^2} d\omega' \quad (6.4a)$$

$$\epsilon_2(\omega) = -\frac{2\omega}{\pi} P \int_0^{\infty} \frac{\epsilon_1(\omega') - 1}{\omega'^2 - \omega^2} d\omega' \quad (6.4b)$$

The WVASE32 software package allows one to use a graphical interface to provide initial guesses for the various fit parameters. At times this required multiple oscillators to best fit the predicted ϵ_2 function. Once this has been
745 set, all of the parameters affecting ϵ_2 (A, E_0, C, E_g) are marked to be included in the fit. The software is then instructed to perform a best-fit of the oscillator to ϵ_2 . Once this operation completes, the software is set to fit to ϵ_1 and only the value of the ϵ_1 offset is allowed to be fit. Finally, the software is set to optimize vs both ϵ_1 and ϵ_2 , and all parameters are included. This completes
750 the initial setup of the oscillator model.

Finally, the model is set to also allow the layer thickness to be fit and a general fit to the entire experimental dataset is performed. This provides the best guess to the physical values of the film. The thickness calculated by this procedure matches very closely to measurements performed by other methods
755 (e.g. SEM imaging or AFM measurement of a lithographically created step).

If similar deposition parameters are utilized, it is possible to save the parameterized model for later use. This allows the analysis to be streamlined when the material is expected to remain constant, for example if tests of deposition at different layer thicknesses are performed. In this case, the material
760 would have optical behavior very similar to the initial sample, and the oscillator model would be sufficiently close to valid parameters to be used directly for fits. All that would need to be adjusted initially would be the estimated layer thickness. If the fit fails to produce useful data, such as unreasonable values for any of the parameters or very large confidence intervals, it is recommended
765 to proceed with the entire standard analysis procedure.

Further analysis can be performed to estimate the bandgap of the layer, via Tauc plot analysis. The method requires the calculation of the absorption coefficient (α) from the value of k for the layer (see equation 6.5). α is usually provided in terms of cm^{-1} , so if the wavelength is provided in nanometers
770 a corresponding factor of 10^7 must be incorporated as well. Subsequently, a Tauc plot is constructed using a combination of α and the photon energy. For direct bandgap materials the Tauc parameter is given by $(\alpha E_{ph})^2$. If the bandgap is of the indirect type, the function is changed to $\sqrt{\alpha E_{ph}}$. The bandgap parameter matches well to literature values (when using standard
775 samples of well defined materials, such as a thin layer of titania). It must be noted that the bandgap that is calculated is the overall bandgap of the layer, which may be a combination of multiple phases or materials.

$$\alpha = \frac{4\pi k}{\lambda} \quad (6.5)$$

Experimental data sets, the resulting fitted models, and Tauc analyses for selected samples are presented in appendix A.7 on page 53.

780 6.3 Composition Analysis

In order for the desired phase to be preferred, without any impurity phases precipitating, it is important to be able to control the stoichiometry of the produced film. Previous reports have shown that there is a close relationship between the composition of the film and the final resultant phase (see figure 6.2
785 on the next page).⁴

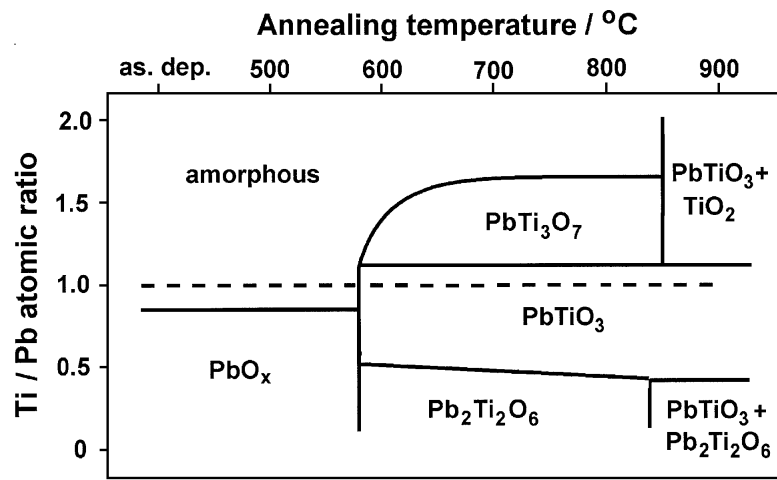


Figure 6.2: Graphic illustrating preferred phase of an annealed film at a range of stoichiometric ratios and annealing temperatures. A slight excess of Pb in the system is expected to help stabilize the perovskite PbTiO_3 phase.⁴

6.3.1 Energy-Dispersive X-Ray Spectroscopy

6.3.2 X-Ray Fluorescence Spectroscopy

X-ray Fluorescence was the primary method for determining the composition of the deposited films. Analysis is performed much

790 Initial calibration of the system is critically important to acquiring accurate measurements. Calibration is performed using a pair of standard samples of known composition, which include all elements that are to be quantified. For this study, a pellet of commercially prepared PbTiO_3 powder and a thin film of $\text{PbZr}_{0.52}\text{Ti}_{0.48}\text{O}_3$.

795 6.4 X-Ray Diffraction

6.4.1 Grazing Incidence XRD

For each sample, the value of ω was set to be 80% of the film's critical angle which was determined prior to the scan.

Chapter 7

800 Results

As discussed, the goal of this study was to determine methods for atomic layer deposition of ferroelectric oxides. In the process of realizing this goal there were a number of different areas of study. The first is the analysis of thermal and chemical behavior of the various potential precursors, during 805 which TGA and DSC were primarily used (see [6.1 on page 27](#)). Secondly, the analysis of the film growth behavior under various conditions, this was primarily measured and analyzed using the ellipsometric techniques discussed earlier (see [6.2 on page 27](#)). Third, the film deposition needed to be tuned to produce films with a stoichiometric composition, as this was expected to 810 produce films which would crystallize into the desired perovskite phase, see section [6.3 on page 32](#) for the methods used for this characterization. Fourth, the phase of the crystallized film was analyzed in detail to determine behavior of the films post-annealing. XRD was used extensively for this task (see [6.4 on page 33](#)).

815 7.1 Thermal Analysis

While a viable titanium precursor was well identified in literature as well as experimentally, as was the oxidizers that were used, there was no such universally accepted chemical used in ALD to provide a source of lead. The primary issue was either a lack of chemical stability or a undesirably low volatility in 820 the compounds that currently were being used. TGA and DSC was performed on a number of potential candidates (see ?? on page ?? for more details) in order to gauge the performance of these materials.

7.1.1 Thermogravimetric Analysis

Thermogravimetric analysis allows for the estimation and comparison of 825 volatility between multiple samples. It was used in this study to compare $\text{Pb}(\text{HF}\text{Ac})_2$ and $\text{Pb}(\text{TMHD})_2$, primarily their individual volatilities — by analyzing the mass loss at various temperatures — and whether or not there are

indications of imperfect evaporation. The data collected for these materials can be found in section A.5.1 on page 46.

830 By analyzing the TGA curve for $\text{Pb}(\text{HFAc})_2$, found in figure A.2a on page 46, there are a number of features that are immediately noticeable. First of these is the multiple stages of evaporation present in the curve. These occur at approximately 170, 190, and 230°C. A TGA curve for a material that is purely evaporative, e.g. pure water, will have a single step in the curve. Additional steps indicate that other processes are activating, and causing changes 835 to the compound affecting the mass loss.

More detail can be seen by performing a derivation on the TGA curve, giving the mass loss rate. This plot can be found in figure A.2b on page 46. This plot shows a shoulder on the primary evaporative peak, and then another peak 840 starting at around 170°C and peaking at 190°C. The shoulder indicates that even during the evaporation of most of the material, a secondary mechanism is activating causing additional mass loss.

7.1.2 Differential Scanning Calorimetry

7.2 Ellipsometry

845 7.3 Composition

7.4 X-Ray Diffraction

Chapter 8

Conclusions

8.1 Future Work

- 850 Optimize consistency
- Doped materials
- Other material systems (BFO, BST, etc.)

Bibliography

- [1] J. A. Woollam Co., Inc. M-2000 ellipsometer. http://www.jawoollam.com/m2000_home.html.
855
- [2] J. A. Woollam Co., Inc. *Guide to Using WVASE32*, 2009.
- [3] Jr. G. E. Jellison and F. A. Modine. Parameterization of the optical functions of amorphous materials in the interband region. *Applied Physics Letters*, 69(3):371–373, 1996.
- 860 [4] J Harjuoja, A Kosola, M Putkonen, and L Niinisto. Atomic layer deposition and post-deposition annealing of PbTiO thin films. *Thin Solid Films*, 496(2):346–352, February 2006.
- [5] iXRF Systems, Inc. fx-sem xrf system. <http://www.ixrfsystems.com/products/xrf/bulk-xrf>.
- 865 [6] Cambridge NanoTech, inc. Savannah s100 series ald. <http://www.cambridgenanotech.com/products/savannah.php>.

Appendix A

Supplemental Information

A.1 List of Chemicals

870 Ph₄Pb
Ti—o—i—Pr
Pb(TMHD)₂
Pb(HFAc)₂
Buffered HF

875 N₂
O₂
O₃
H₂O
IPA

880 Acetone

A.2 List of Samples

Table A.1: A list of samples used during the course of this project.

Temperature (°C)	Pb:Ti Deposition Ratio	Run Number	Substrate Type	Super- cycles	Total cycles	Anneal Type	Anneal Temp (°C)	Anneal Time	XRD	Notes
200	1:1	3	Si	250	500	Oven	-	-	N	Blah
200	1:2	2	Si	250	750	Oven	-	-	N	
200	3:1	30	- Si - Pt	160	640	Oven	-	-	N	
250	1:1	0	Si Si	625	1250	Oven - Amb - Oven - Amb -	650 900	2h 2h	Y Y	Green sample, no apparent change Sample turned a purplish blue color, still shiny but not as shiny as untreated Small chip, no longer shiny, odd structures present after annealing (via opt. micro), appears to have formed nano-rods after anneal (see SEM images). Made more samples in RTA at 600, 700, 800, 900 °C, similar results on all but 600 °C test
250	1:1	1	Si	475	950	RTA	900	10m	N	
250	1:2	6	Si	250	750				N	
250	3:1	13	Si	250	1000				N	Tried 60s between Pb pulses, needs a little more. Sample appeared uniform except for one spot (effect of tape?). Yellow spot has different thickness (23.5nm) and different osc. parameters.
250	3:1	16	Si	150	600	RTA	650	1m	N	
250	3:1	19	- Si - Pt	100	400				N	Replaced precursor prior to this run.
250	3:1	20	Si Pt	200	800	- Fast Oven	- 650	-	N	Runs appear to be growing well. Spectacular colonization on the reactor surface where platinum was deposited.
250	3:1	21	- Si - Pt	150	600	- Fast Oven	- 650	1m	Y	
250	3:1	22	- Si - Pt	150	600	- Fast oven	- 650	1m	Y	Discolored, not homogeneous across sample..

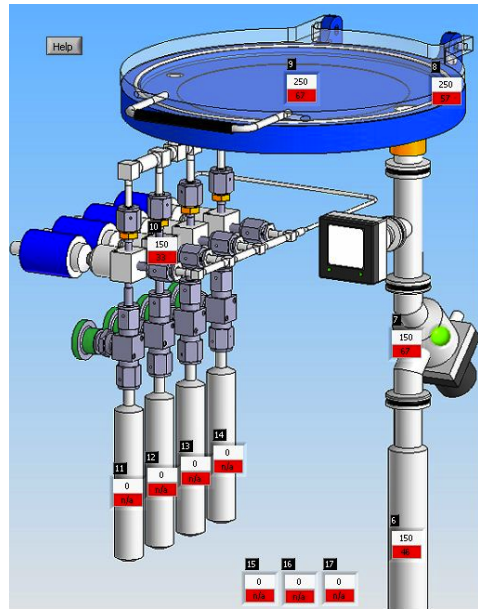
Table A.1: A list of samples used during the course of this project.

Temperature (°C)	Pb:Ti Deposition Ratio	Run Number	Substrate Type	Super- Cycles	Total Cycles	Anneal Type	Anneal Temp (°C)	Anneal Time	XRD	Notes
250	3:1	23	- Si - Pt	200	800	- Fast oven	-	-	-	-
250	3:1	24	- Si - Pt	200	800	-	-	-	N Y	-
250	3:1	25	- Si - Pt	60	240	-	-	-	N -	-
250	2:1	26	- Si - Pt	80	240	-	-	-	N -	-
250	5:2	27	- Si - Pt	110	770	-	-	-	N -	-
250	3:1	28	- Si - Pt - STO	120	480	-	-	-	N -	-
250	3:1	29	- Si - Pt	50	200	-	-	-	N -	-
250	2:1	18	Si	200	600				N	Might be running low on Pb(TMHD)2 precursor, going to add some more this afternoon
300	1:1	4	Si	250	500				N	
300	1:2	5	Si	200	600				N	
300	2:3	9	Si	175	875				N	May have gotten recipe timing wrong, might have to re-do this test...
300	3:2	10	Si	50	250				N	
300	3:1	11	Si	150	450				N	

A.3 ALD Reactor Diagram



(a) Photograph



(b) Schematic Diagram

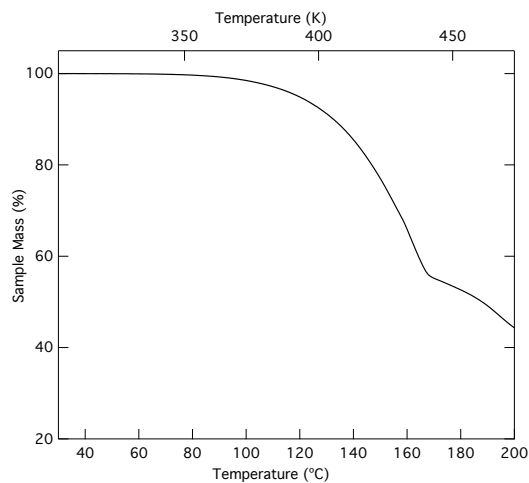
Figure A.1: Cambridge NanoTech, inc. Savannah S100 ALD reactor. Precursors are stored in heated cylinders, flow up to the reaction zone, and byproducts are pumped out of the vacuum line on the right side. Each zone can be individually temperature controlled.

A.4 Recipes for S100 ALD System

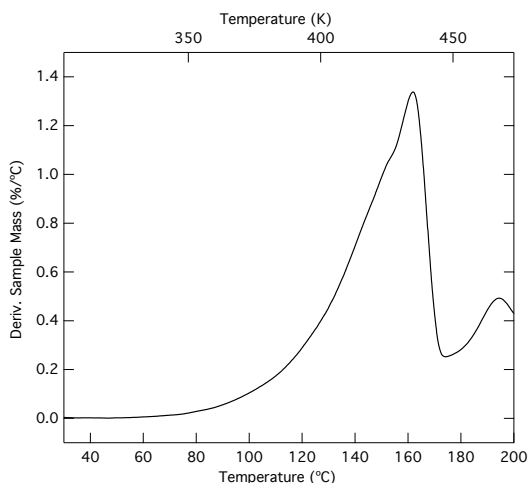
Some of these recipes (HfO_2 , Pt, and TiO_2) were provided courtesy of
885 Cambridge NanoTech, inc.⁶

A.5 Thermal Analysis Results

A.5.1 Thermogravimetric Analysis



(a) Mass vs. Temperature



(b) Derivative of Mass vs. Temperature

Figure A.2: Plots of the results from TGA experiments on $Pb(HF\text{Ac})_2$. The plot shown in (a) gives the raw data showing the current mass as a function of temperature. (b) gives the same data, transformed to show the derivative of mass. Thus (b) shows the rate of mass loss at a given temperature. Initial sample mass: 6.092 mg

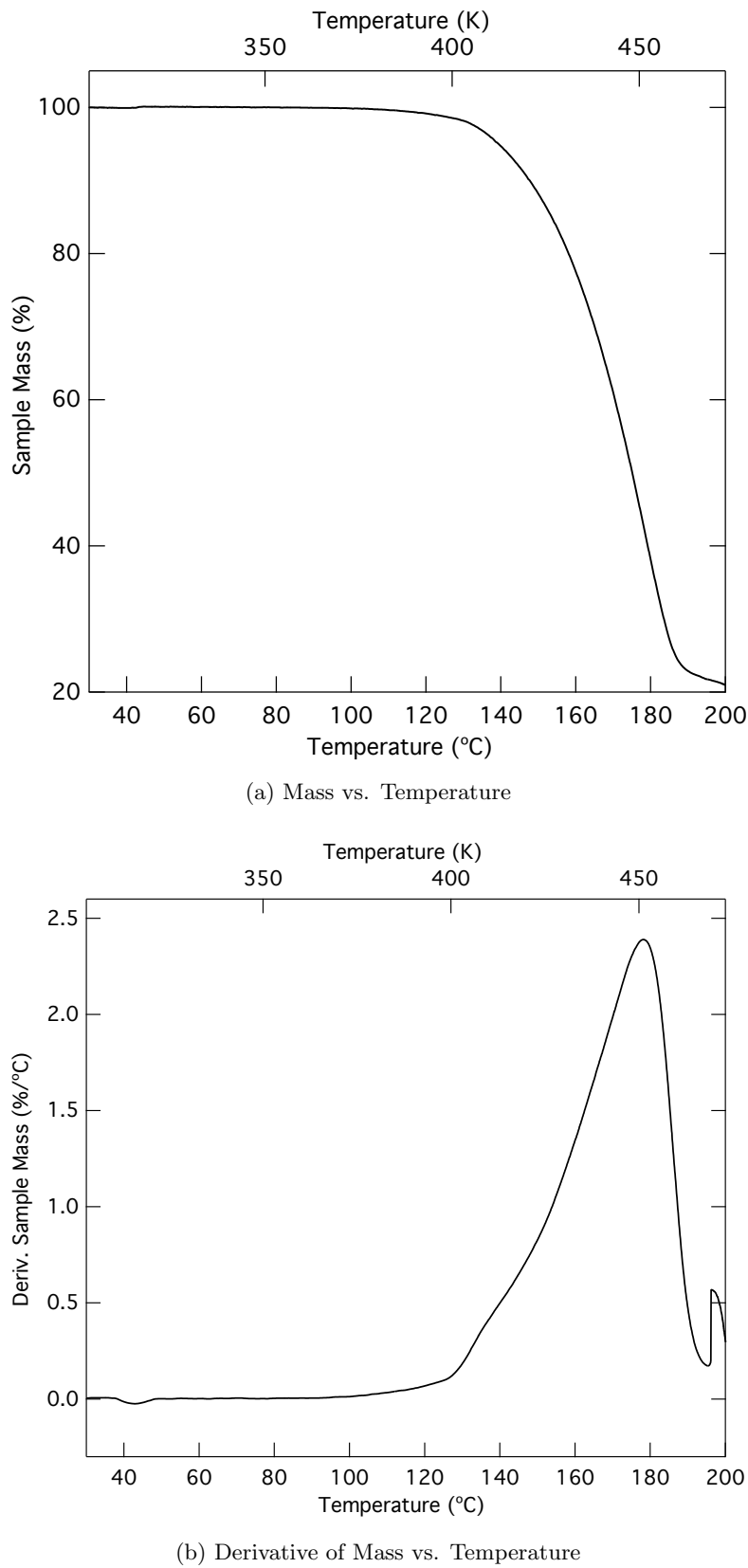


Figure A.3: Plots of the results from TGA experiments on $\text{Pb}(\text{TMHD})_2$. As in figure A.2 on the preceding page, (a) presents the actual mass as a function of temperature, while (b) gives the derivative of that function. Initial sample mass: 3.719 mg

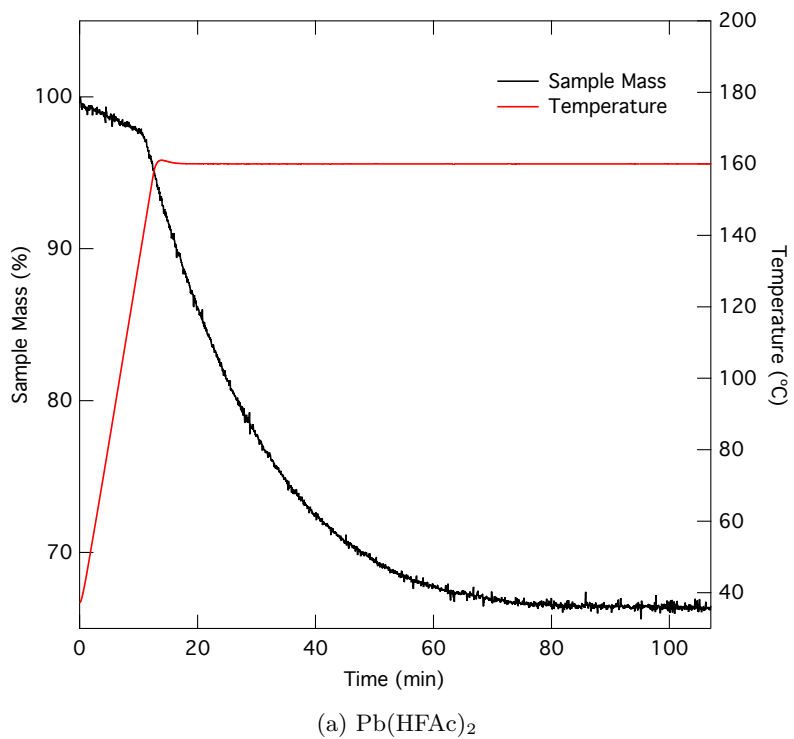
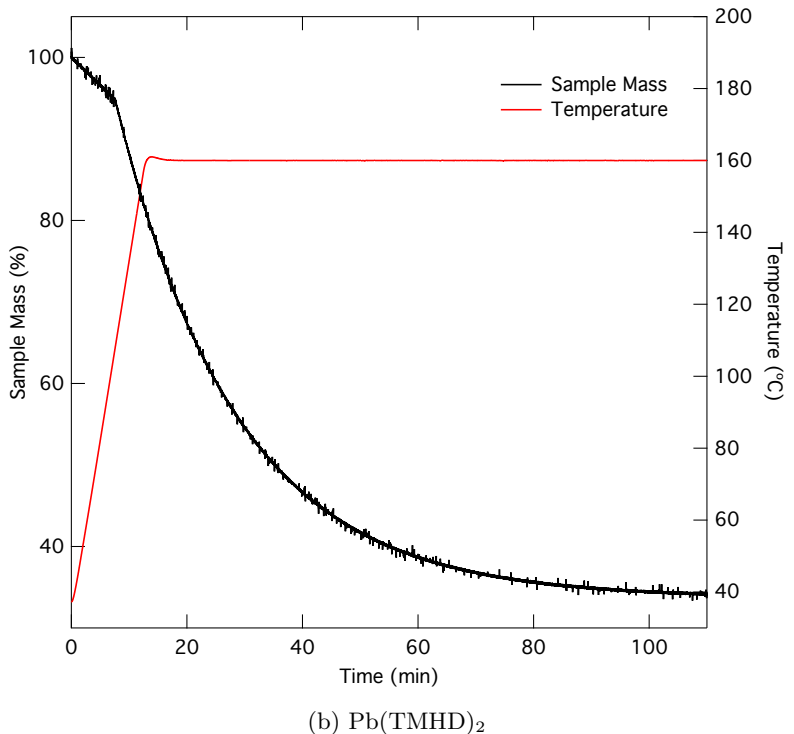
(a) $\text{Pb}(\text{HFAc})_2$ (b) $\text{Pb}(\text{TMHD})_2$

Figure A.4: Plots of the results from ramp-and-hold TGA experiments designed to investigate residual material after complete evaporation at a given temperature. From the TGA experiments seen above (figs. A.2 on page 46 and A.3 on the previous page), a common temperature of 160°C was chosen for this experiment. Sample sizes were 3.921 mg and 4.381 mg for $\text{Pb}(\text{HFAc})_2$ and $\text{Pb}(\text{TMHD})_2$ respectively.

A.5.2 Differential Scanning Calorimetry

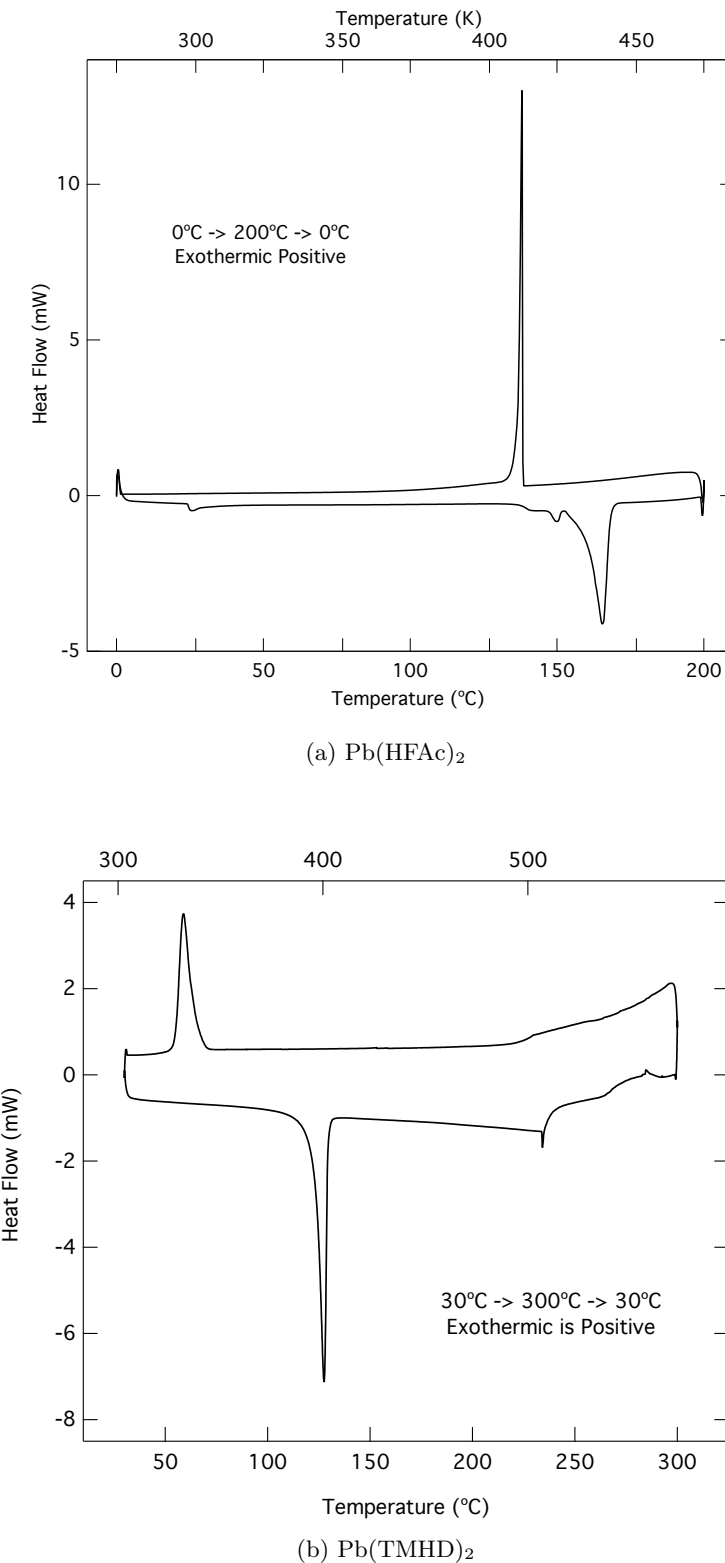


Figure A.5: This plot shows results from DSC experiments carried out during the course of this project. (a) shows the results from analyzing the $\text{Pb}(\text{HFAC})_2$ compound. (b) gives the data from $\text{Pb}(\text{TMHD})_2$. Exothermic (heat release) flow is positive in both plots.

A.6 Composition Results

Table A.2: Calculated compositions of selected samples, determined via XRF.

Run #	Substrate	Composition (%)		
		Lead	Titanium	Ti:Pb Ratio
0	SiO ₂	55.99	44.01	0.786
1	SiO ₂	55.00	45.00	0.809
13	SiO ₂	53.96	46.04	0.853
16	SiO ₂	49.45	50.55	1.022
19	SiO ₂	65.87	34.13	0.518
	Pt-Si	42.86	57.14	1.333
20	SiO ₂	56.52	43.48	0.769
	Pt-Si	51.43	48.57	0.944
21	SiO ₂	69.60	30.40	0.437
	Pt-Si	56.08	43.92	0.783
22	SiO ₂	67.64	32.36	0.478
	Pt-Si	56.06	43.94	0.784
23	SiO ₂	66.89	33.11	0.495
	Pt-Si	49.06	50.94	1.038
24	SiO ₂	68.96	31.06	0.450
	Pt-Si	62.16	37.84	0.609

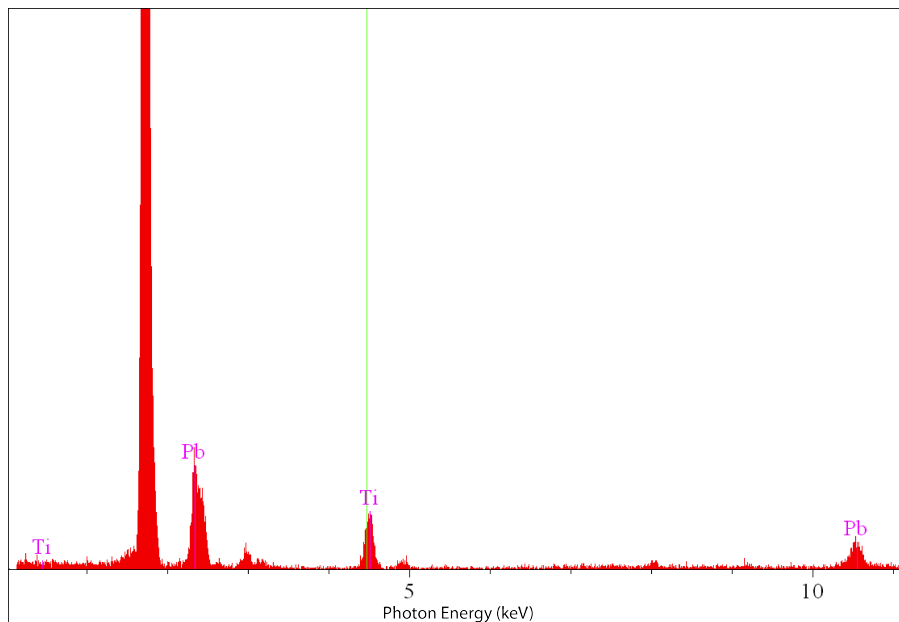


Figure A.6: The XRF spectrum collected from deposition run #0.

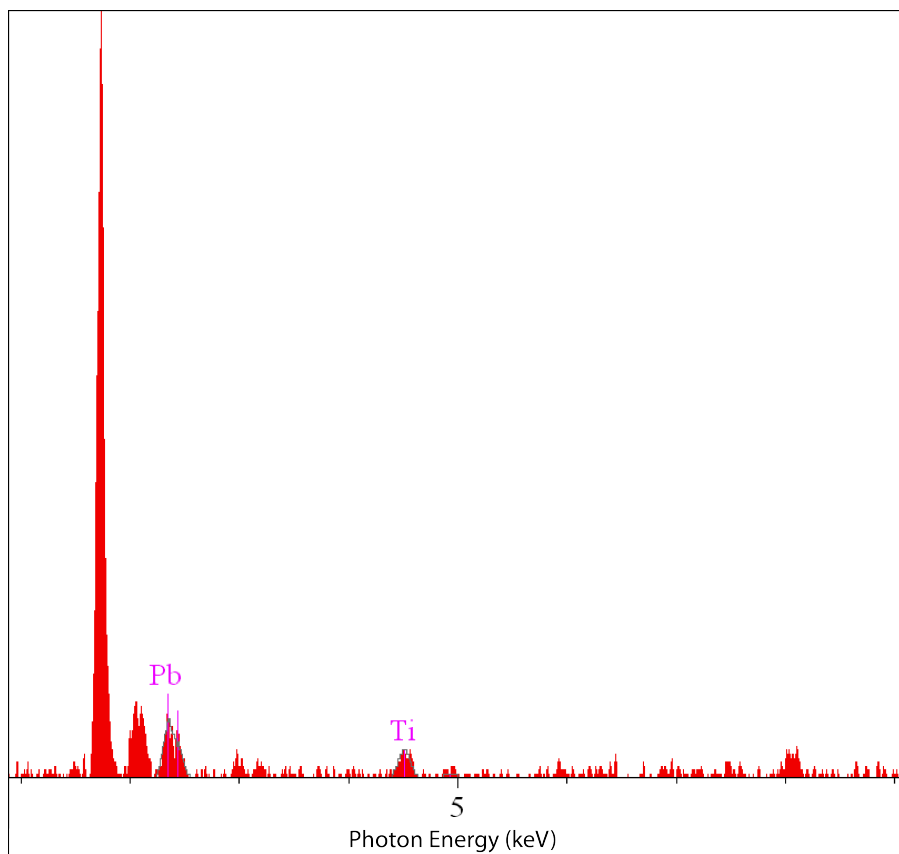


Figure A.7: The XRF spectrum collected from deposition run #20 deposited on platinized silicon. The peak between the substrate and Pb is that of Pt.

⁸⁹⁰ **A.7 Ellipsometry Results**

Table A.3: Variables used to produce the model fit for PTO #0 seen in fig. A.8 on the next page.

Layer	Variable	Thickness (nm)	Value
2. T-L Osc.		81.56	
	Amp ₁		12.662
	E _{n1}		4.604
	C ₁		1.351
	E _g		0.856
	E ₁ offset		2.491
1. SiO ₂		203.69	
0. Si		Substrate	

Table A.4: Variables used to produce the model fit for PTO #20 seen in fig. A.10 on page 56.

Layer	Variable	Thickness (nm)	Value
3. T-L Osc.		88.77	
	Amp ₁		36.542
	E _{n1}		4.505
	C ₁		1.298
	E _g		2.071
	E ₁ offset		3.619
2. Pt		15.052	
1. SiO ₂		1.103	
0. Si		Substrate	

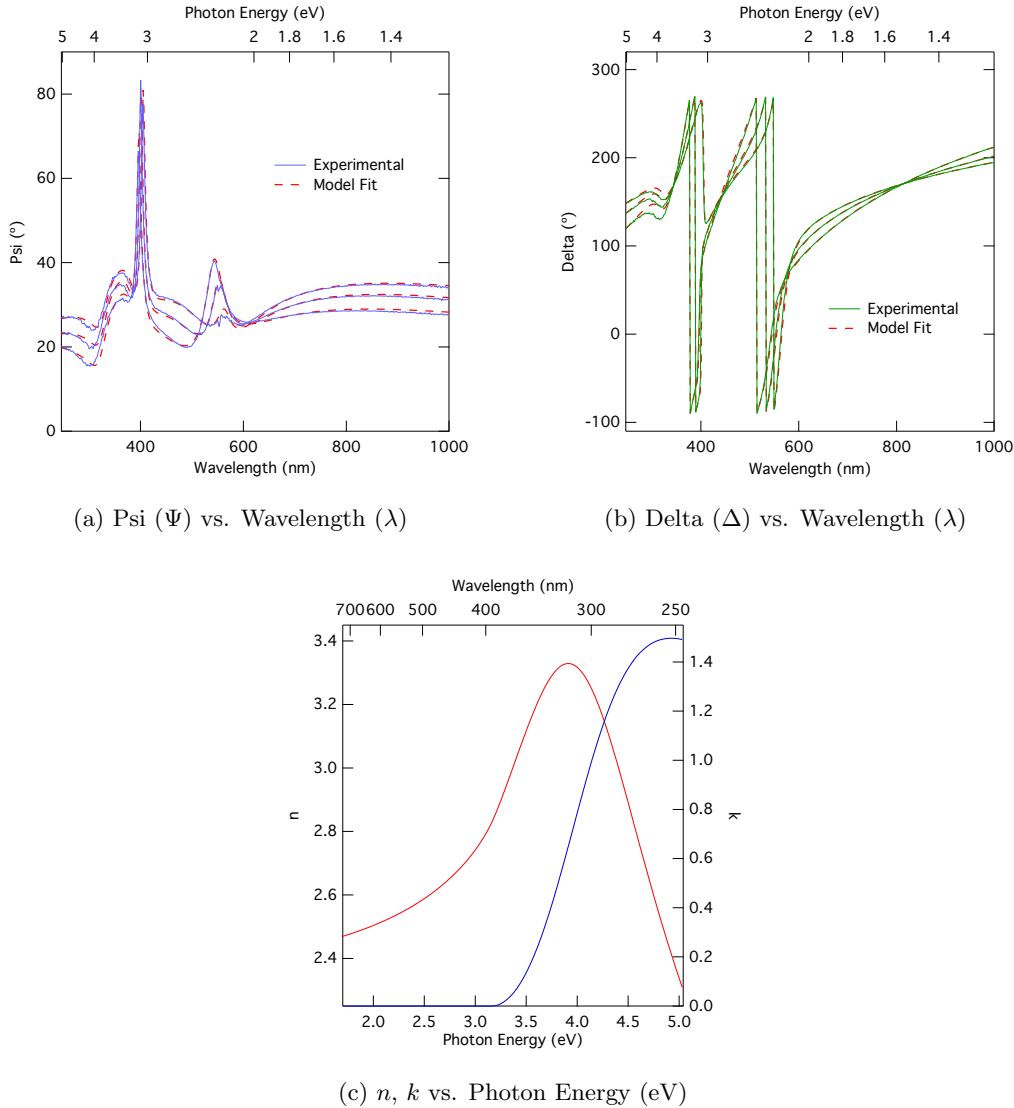


Figure A.8: The set of plots shown above show the results from ellipsometric analysis on sample #0 (see table A.1 on page 43) grown on a silicon wafer and subsequently annealed. (a) and (b) show the data and the modeled fit from the experiment. (c) shows the components of the complex index of refraction (\tilde{n}), n and k . Band gap estimation was performed using the values of k . The highlighted portion of k is the nearly linear region used in this analysis.

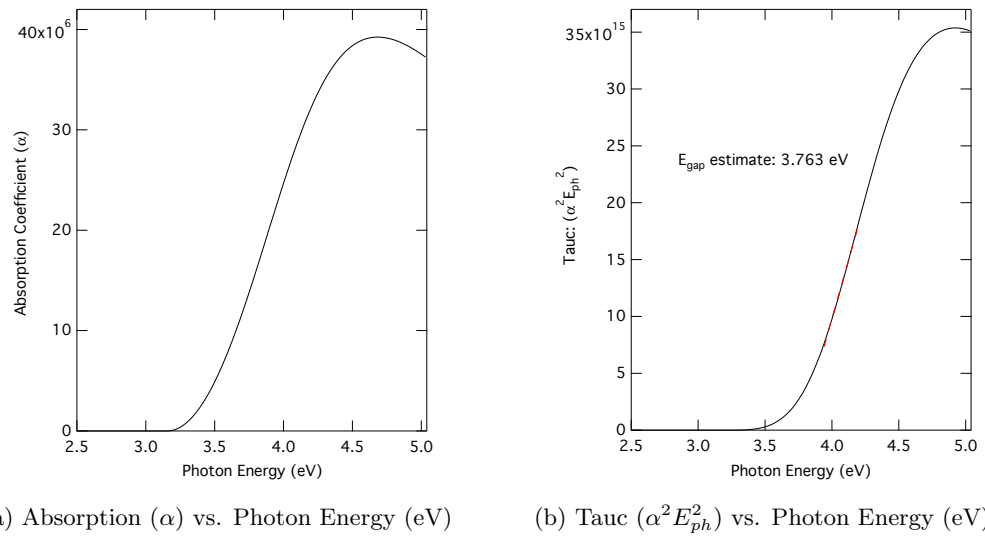


Figure A.9: Tauc analysis used to determine the bandgap of PTO #0. (a) shows the values of the absorption coefficient (α) calculated from k (seen in figure A.8c on the preceding page). (b) shows the Tauc plot, the linear region can provide an estimate of the bandgap of the material.

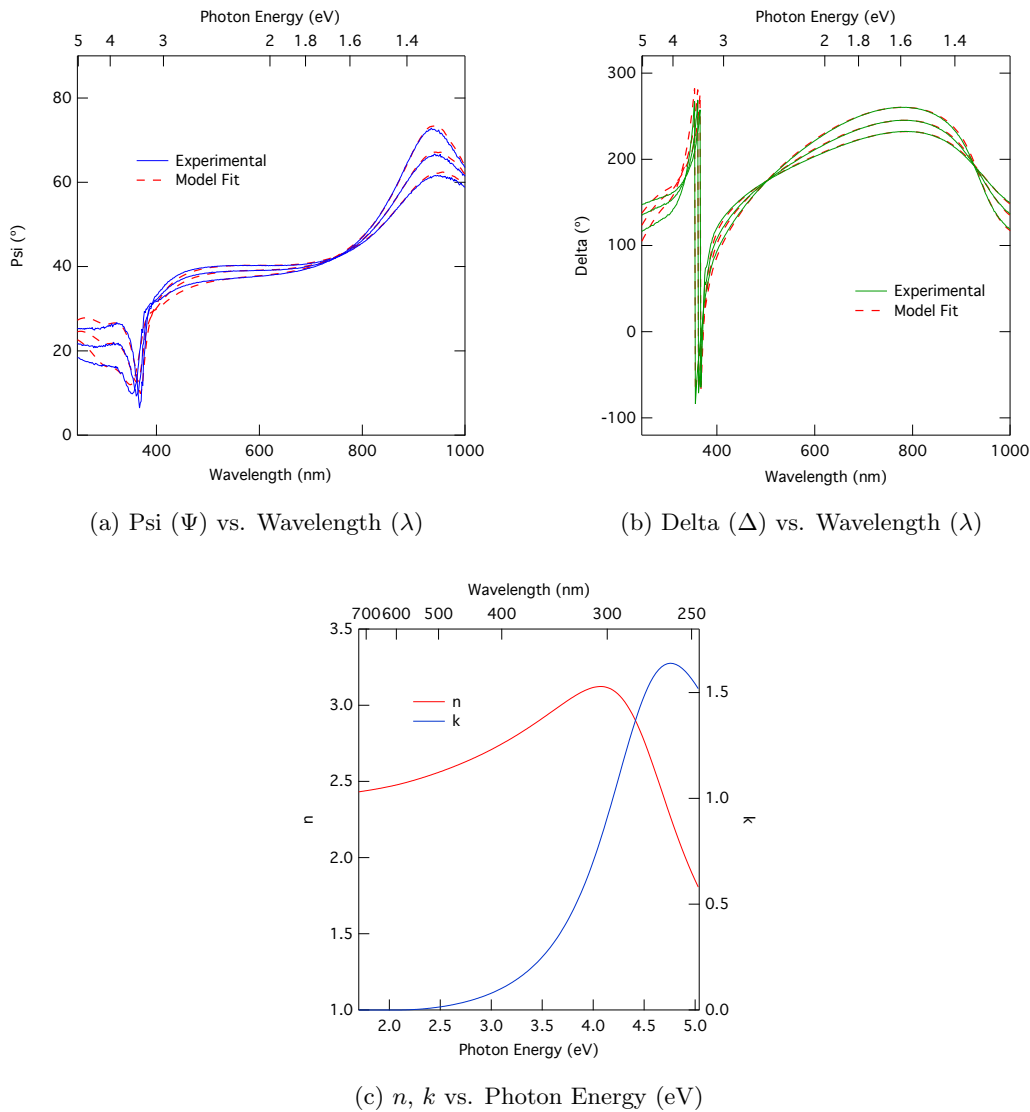


Figure A.10: Results of ellipsometric analysis on sample #20, deposited on a platinized silicon substrate. As in fig.A.8, (a) and (b) show the experimental data and model fits of psi and delta (respectively). (c) gives the plot of calculated n and k . For model parameters, see table A.4 on page 53

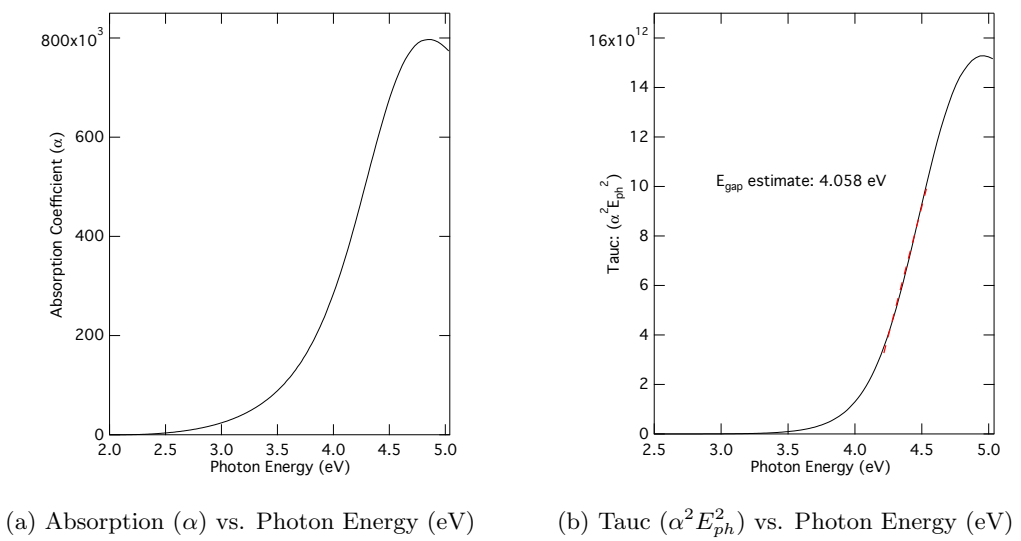


Figure A.11: Tauc analysis

A.8 XRD Results

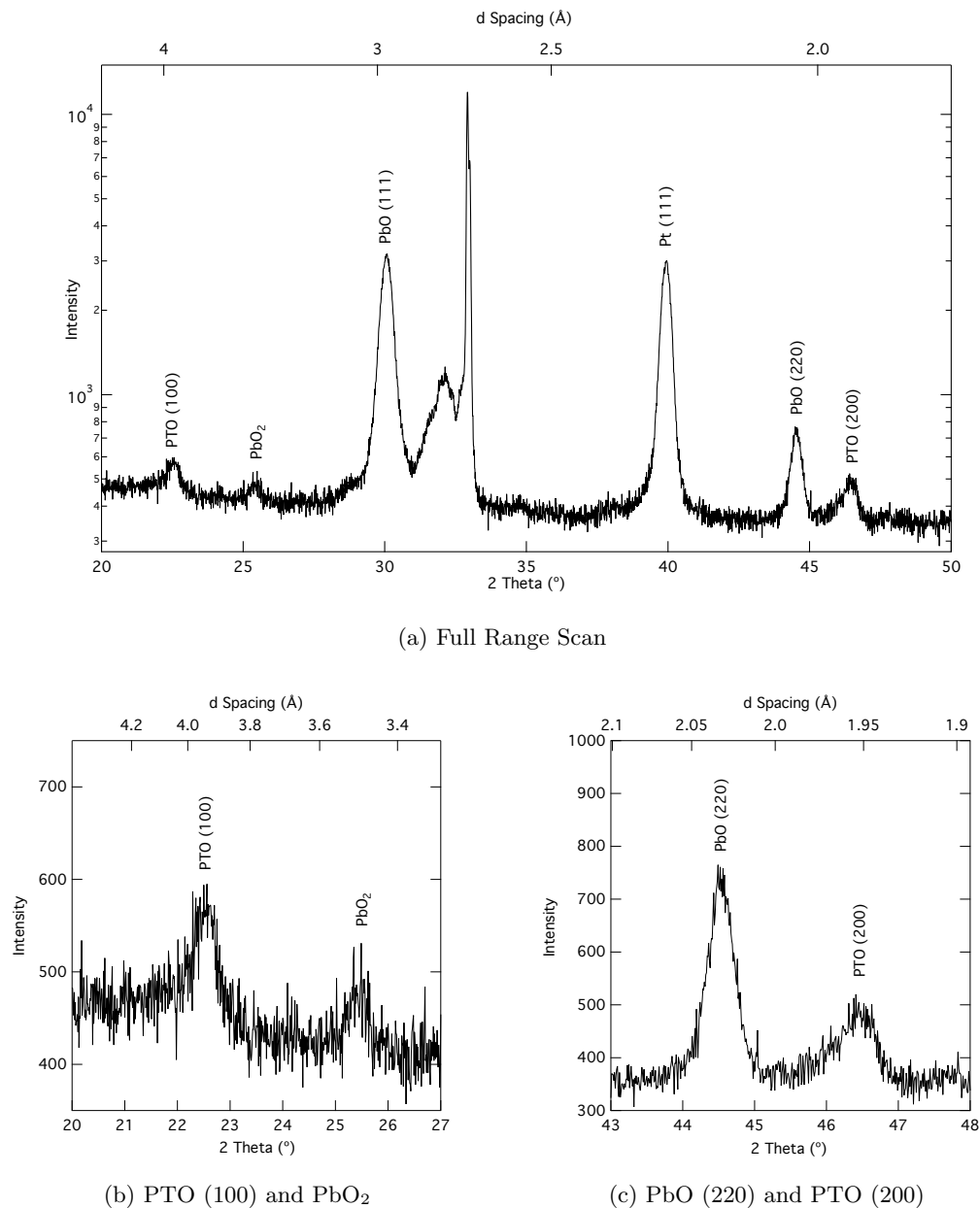


Figure A.12: Caption caption caption